International Journal of Bifurcation and Chaos, Vol. 5, No. 3 (1995) 595–635

BURSTING, SPIKING, CHAOS, FRACTALS, AND UNIVERSALITY IN BIOLOGICAL RHYTHMS

TERESA REE CHAY and YIN SHUI FAN
Department of Biological Sciences, University of Pittsburgh, Pittsburgh, PA 15260, USA

YOUNG SEEK LEE
Department of Biochemistry, Hanyang University, Seoul, Korea

Received May 19, 1994; Revised June 13, 1994

Biological systems offer many interesting examples of oscillations, chaos, and bifurcations. Oscillations in biology arise because most cellular processes contain feedbacks that are appropriate for generating rhythms. These rhythms are essential for regulating cellular function. In this tutorial review, we treat two interesting nonlinear dynamic processes in biology that give rise to bursting, spiking, chaos, and fractals: endogenous electrical activity of *excitable cells* and Ca^{2+} releases from the Ca^{2+} stores in *nonexcitable cells* induced by hormones and neurotransmitters. We will first show that each of these complex processes can be described by a simple, yet elegant, mathematical model. We then show how to utilize bifurcation analyses to gain a deeper insight into the mechanisms involved in the neuronal and cellular oscillations. With the bifurcating diagrams, we explain how spiking can be transformed to bursting via a complex type of dynamic structure when the key parameter in the model varies. Understanding how this parameter would affect the bifurcation structure is important in predicting and controlling abnormal biological rhythms. Although we describe two very different dynamic processes in biological rhythms, we will show that there is universality in their bifurcation structures.

1. Introduction

There is a growing interest in nonlinear dynamics in biology, especially in the area of rhythms and chaos [Rapp, 1993]. This interest stems partly from the realization that some disorderly behavior in biological rhythms seems to be governed by deterministic rules. As James Gleick [1987] explains in his best-selling book, "CHAOS — Making a New Science," chaos offers a way of seeing order and pattern where formerly only the random, the erratic, and the unpredictable were observed. This opens the possibility that abnormal rhythmic activity in biology can be explained by theory of nonlinear dynamics. In order to systematically study abnormal rhythmic activity in biology, however, modeling is needed. In the past, electrical phenomena in excitable cells and cellular dynamic processes in nonexcitable cells captured our attention, and we have formulated mathematical models that explain the basic mechanisms involved in rhythmic activity of these two biological processes. *Excitable cells* are the cells whose plasma membrane contains voltage-dependent ion channels, and thus the membrane potential of these cells responds when chemicals which modify the key ion channels are added to the medium. On the other hand, *nonexcitable cells* are electrically quiescent, but the intracellular calcium concentration of these cells becomes oscillatory upon addition of certain neurotransmitters or hormones. Although both models describe very different biological

phenomena, they give rise to spiking, bursting, chaos, and fractals, when the key parameter in the model is varied. Why such universal behaviors arise from these biological models can be understood by constructing bifurcation diagrams using software such as AUTO [Doedel, 1981; Doedel & Kernevez, 1986; Doedel *et al.*, 1991a, b].

Section 2 of this review deals with endogenous electrical activity of neurons. Figure 1 describes types of bursting observed in the membrane potentials of *Tritonia* neurons (frame a) and *Aplysia* neurons (frame *b*). As shown here, a burst consists of a rapid sequence of action potentials at regular intervals separated by a silent period during which the cell membrane hyperpolarizes. The fast action potentials are referred to as spikes. The time scale of a burst is on the order of tens of seconds while the spikes have a millisecond time scale. Under certain circumstances, however, these bursts become chaotic. How chaos may affect neurobiology is a very important theoretical problem since it may help predict the onset of neurodisorders such as epileptic seizures and suggest the means to control them. But to determine the limitations and applications of nonlinear dynamics to neurobiology, it is necessary to study the genesis of chaotic activity under well controlled conditions. A bifurcation analysis is the right method to employ in achieving this purpose, since it gives a lucid picture on how the dynamic structure changes when a bifurcation parameter varies.

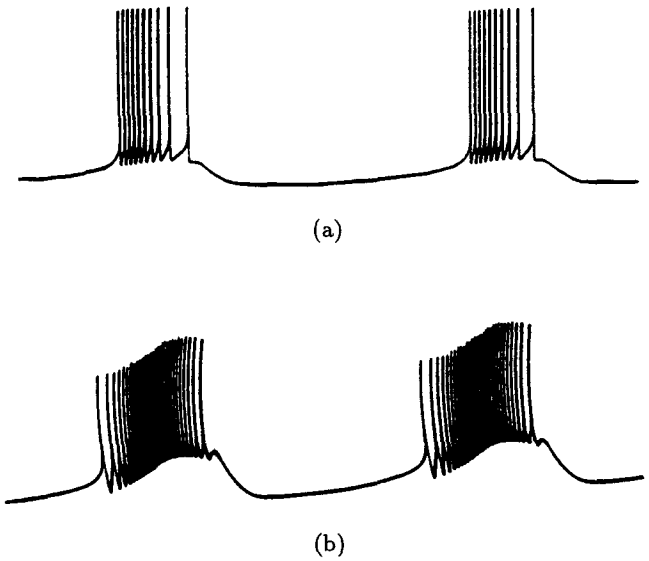

Fig. 1. Types of electrical burstings in excitable cells. (a) *Tritonia* neuron. (b) *Aplysia* neuron.

With the two types of neuronal models presented in this section, we will demonstrate how a small change in the conductance of the key channel in the plasma membrane can cause chaos in the rhythmic activity. These models predict several types of chaos, some of which have been observed in examples of one-dimensional discrete systems, e.g., period-doubling chaos [May, 1976] and interior crisis [Grebogi & Ott, 1983]. But there are a few new features which are unique to the excitable models, an example being a spike splitting route which leads to an inverse Feigeinbaum scenario [Feigenbaum, 1983, 1987]. This spike splitting route begins with a spike which rides on a threshold unstable oscillation. The spike then splits into two, three, and so on, until bursting-chaos sets in. Bursting-chaos sets in only when the number of attractors is an odd number. It then transforms to spiking-chaos at the crisis transition. Spiking-chaos leads to an inverse period doubling cascade until it reaches a depolarized quiescent state. In addition to this interesting scenario, in the transition zone where n-spikes are split into $n + 1$ spikes, there arise complex oscillatory modes that contain several interesting types of chaos and a periodic state between them.

Section 3 deals with the intracellular calcium oscillations in a wide variety of nonexcitable cells (e.g., hepatocytes and oocytes). These cells generate repetitive changes in their intracellular Ca^{2+} concentration, $[Ca^{2+}]_i$, when a certain agonist — a neurotransmitter or a hormone — is added to the medium. Figure 2 shows the types of intracellular Ca^{2+} oscillations that arise in nonexcitable cells. At first, nonexcitable cells were thought to be "dull" because they are electrically nonresponsive cells, and thus little attention was paid by those scientists engaged in oscillatory phenomena. Seminal work by Cobbold and his collaborators changed the image of nonexcitable cells; they reported that hepatocytes [Wood *et al.*, 1986] and oocytes [Cuthbertson and Cobbold, 1985] can also give rise to oscillatory signals (in a form of $[Ca^{2+}]_i$) very similar to action potential in excitable cells. Since then, the oscillation in $[Ca^{2+}]_i$ has been discovered in many other nonexcitable cells [Berridge, 1989; Putney & St. J. Bird, 1993]. These oscillations are due to the release of calcium ions from the intracellular calcium stores (e.g., endoplasmic reticulum and calcium-induced calcium-releasing stores). The pattern of $[Ca^{2+}]_i$ oscillation is agonist specific in that some agonists can generate a spike like $[Ca^{2+}]_i$ oscillation while others can generate a burst-like

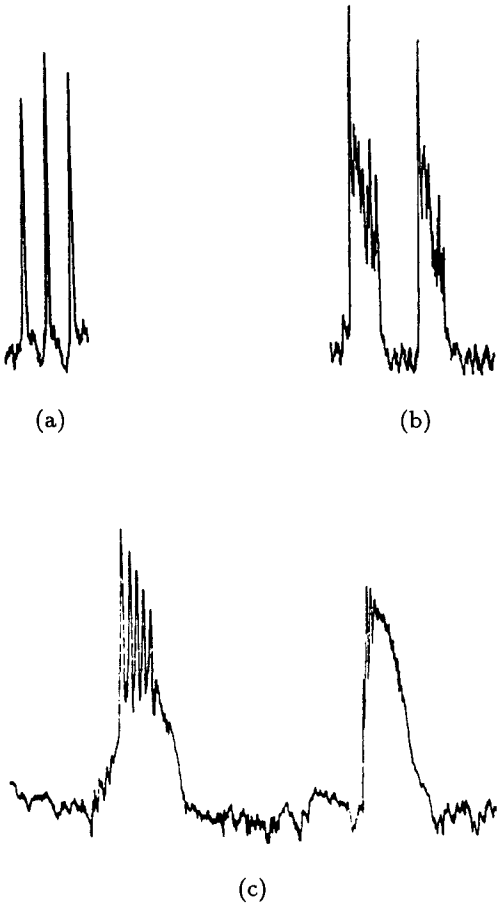

Fig. 2. Types of intracellular calcium oscillations measured with aequorin. Free Ca^{2+} changes in (a) hepatocyte induced by phenylephrine, (b) the same cell induced by adenosine triphosphate (ATP), and (c) mouse oocytes during fertilization.

oscillation. Using a mathematical model presented in Sec. 3.1, we will show why such patterns may occur. We will also show that the bursting model of a nonexcitable cell behaves very similar to that of the excitable cell, when the key parameter in the model is varied. These similarities include a spike splitting scenario and complex oscillatory modes in the transition zone between the n-spike bursting and the $n+1$-spike bursting.

The above studies involve a steady application of the agonist. Under *in vivo* conditions, however, the brain releases neurotransmitters and hormones in a pulsitile fashion [Kriebel *et al.*, 1990; Brabant *et al.*, 1992)]. Thus, how nonexcitable cells respond to a pulsitile application of agonists is of great physiological importance. Experiments of Schofl *et al.* [1993] showed in hepatocytes that Ca^{2+} release is blocked when the frequency of periodic pulses of agonist increases. This frequency dependent block recalls the phase-locking response seen theoretically and experimentally in action potentials in excitable cells driven by periodic current pulses [Hayashi, 1982; Matsumoto *et al.*, 1987]. This block also closely resembles Wenckebach rhythms observed in heart patients [Shrier *et al.*, 1987]. We will demonstrate in Secs. 3.4–3.5 that the phase-locking behavior of $[Ca^{2+}]_i$ by the periodic agonist stimulation is fractal and follows universal rules found in other phase-locking systems.

2. Chaos in the Excitable Models of Neurons

To find the origin of rhythmic activity of neurons, it is important to understand the roles of the key ion channels in the plasma membrane. The channels which are believed to participate in electrical activity of neurons are shown in Fig. 3. Neuron cells contain a high concentration of K^+ (140 mM inside and 5 mM outside), a low concentration of Na^+ (20 mM inside and 130 mM outside), and a very low concentration of Ca^{2+} ions (100 nM inside and 2.5 mM outside). The Na^+ and Ca^{2+} channels are voltage-dependent in that they open and allow their respective ions to enter when the membrane is depolarized to about -45 mV from the resting level of about -60 mV. The delayed rectifying K^+ channel also depends on voltage, but it allows K^+ to go out of the cell when the membrane is depolarized. On the other hand, the opening process of the Ca^{2+}-sensitive K^+ channel depends on intracellular Ca^{2+} ion in that it opens and allows K^+ ions to leave the cell only when $[Ca^{2+}]_i$ becomes high. The Na^+/K^+ pump "pumps" three Na^+ molecules from the cell and two K^+ molecules to enter the cell by converting a "high-energy compound" ATP to a "lower-energy compound" ADP. Similarly, the Ca^{2+}-ATPase "pumps" Ca^{2+} ions out of the cell. The Ca^{2+}/Na^+ exchanger exchanges two intracellular Ca^{2+} molecules for three extracellular Na^+ molecules. The endoplasmic reticulum contains high concentration of Ca^{2+} ions and releases Ca^{2+} upon receiving a certain external signal.

There are two hypotheses as to which channel participates in the genesis of the slow wave shown in Fig. 1: (i) a K^+ current that opens slowly during the active spiking phase and (ii) an inward Ca^{2+} current that slowly inactivates during this period. The first hypothesis is based on experimental evidence that there is a small conductance K^+ channel that is insensitive to membrane potential but is

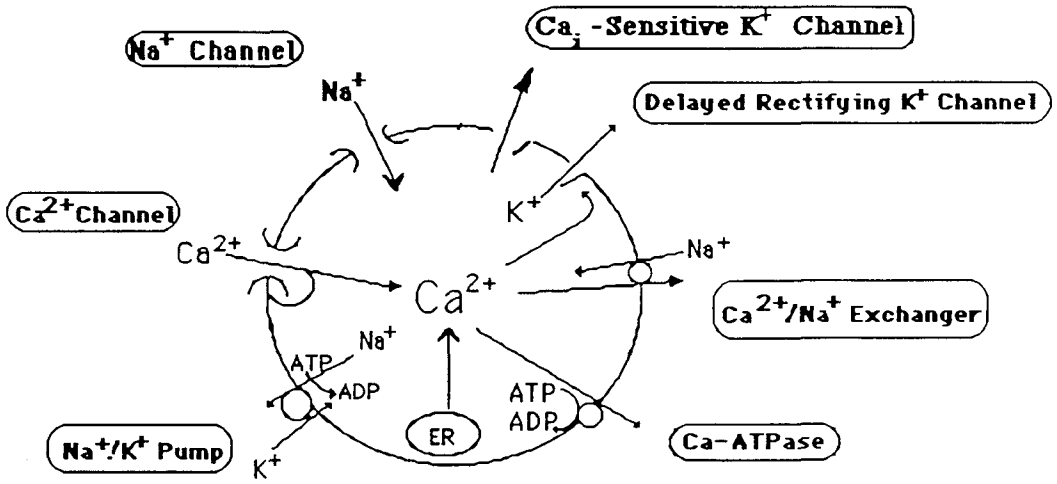

Fig. 3. Ion channels in the plasma membrane of the excitable cell involved in the genesis of bursting. The key channels are the Ca_i^{2+}-sensitive K^+ channel (K–Ca channel) which is activated when the intracellular calcium concentration $[Ca^{2+}]_i$ becomes high, and the Ca^{2+} channel which is inactivated when $[Ca^{2+}]_i$ becomes high. Here, ATP, ADP, and ER stand for adenosine triphosphate, adenosine diphosphate, and endoplasmic reticulum.

sensitive to intracellular Ca^{2+} ions [Gorman, *et al.*, 1981; Ammala *et al.*, 1991]. The second hypothesis is based on experimental evidence that the Ca^{2+} channel in the bursting cells contains an inactivating component which is sensitive to intracellular Ca^{2+} ions [Krammer and Zucker, 1985; Chad & Eckert, 1986]. Thus, it is likely that the bursting neurons may make use of both mechanisms depending on the environmental conditions. In this section, we will treat both hypotheses — a model formulated based on a Ca^{2+}-activated K^+ channel from Sec. 2.1 to Sec. 2.7 and a more elaborated neuronal model based on a Ca^{2+}-blockable Ca^{2+} channel from Sec. 2.8 to Sec. 2.12. Although both models are based on very different mechanisms, we will find that their dynamic structures are very similar (which indicates that there may be universality associated with rhythmic activity of excitable cells).

2.1. *The model based on a Ca^{2+}-activated K^+ channel*

There exist several elaborate models based on the Ca^{2+}-activated K^+ channel in the literature [Plant & Kim, 1976; Plant, 1981; Chay, 1983]. We will treat here a minimal model which captures the essence of the bursting mechanism — the three-variable model described by Chay [1985]. In this model, the first dynamic equation comes from the principle of charge balance, that is, the capacitative current is equal to the negative of the sum of the ionic current components [Hodgkin & Huxley, 1952],

$$-C_m\frac{dV}{dt} = g_1 m_\infty^3 h_\infty (V - V_I) + g_K n^4 (V - V_K) + g_p p (V - V_K) + g_L (V - V_L), \quad (2.1)$$

where V is the membrane potential, g_I, g_K, g_p, and g_L are respectively the maximal conductances of a fast inward current, a fast outward current, a slow outward current, and a leak current, and V_I, V_K, and V_L are their respective reversal potentials. In this model, the third current is responsible for the slow underlying wave.

The first term on the right of Eq. (2.1) is a "fast" inward current carried by Ca^{2+} ions and whose activation gating variable m and inactivation variable h are functions of V as shown below:

$$m_\infty = \frac{\alpha_m}{\alpha_m + \beta_m} \quad \text{and} \quad h_\infty = \frac{\alpha_h}{\alpha_h + \beta_h}.$$

The second term is an outward current carried by K^+ ions. This current is responsible for the downstroke of a spike, where n is the gating variable represented by the following first-order equation,

$$\frac{dn}{dt} = \frac{n_\infty - n}{\tau_n}. \quad (2.2)$$

In the above equation, n_∞ and τ_n are n at the steady state and the relaxation time, respectively,

and are functions of V. Following suggestions by Hodgkin and Huxley [1952], these terms are expressed as follows:

$$n_\infty = \frac{\alpha_n}{\alpha_n + \beta_n} \quad \text{and} \quad \tau_n = \frac{\tau_n^*}{\alpha_n + \beta_n}$$

where the explicit expressions for α_m, β_m, α_h, β_h, α_n, and β_n are given in Appendix I.

The third term is an outward pacemaker current carried by K^+ ions whose probability of opening p (or the fraction of the available Ca^{2+}-sensitive K^+ channels at time t) is a slow dynamic variable which takes the following expression:

$$\frac{dp}{dt} = \frac{m_\infty^3 h_\infty (V_I - V) - k_C p/(1-p)}{\tau_p}(1-p)^2 . \tag{2.3}$$

Since the rate at which p changes with time determines the slow underlying wave, τ_p (the relaxation time constant) controls the periodicity of bursting, i.e., the smaller the value of τ_p, the faster the burst periodicity.

Perhaps, it is worth mentioning that Eq. (2.3) is not the only functional form that generates bursting. See for example Appendix II. The above equation is equivalent to that given in Chay [1985], where in the Chay model of 1985 a slow dynamic variable was manifested via the intracellular calcium concentration $[Ca^{2+}]_i$. In this review, we have replaced $[Ca^{2+}]_i$ by p because recent physiological evidence indicates that $[Ca^{2+}]_i$ changes rather quickly during depolarization [Valdeolmillos *et al.*, 1989], i.e., it may not be a slow dynamic variable. Using the variable p is more consistent with experimental evidence.

To reiterate, this model contains three dynamic variables, V [Eq. (2.1)], n [Eq. (2.2)], and p [Eq. (2.3)]. Here, V is a dependent variable, n is a fast variable that is responsible for the genesis of a spike, and p is a slow dynamic variable responsible for the underlying wave. The basic parametric values are: $C_m = 1$, $g_I = 1800$, $g_K = 1700$, $g_p = 11$, $g_L = 7$, $V_I = 100$, $V_K = -75$, $V_L = -40$, $\tau_n^* = 0.00435$, $\tau_p = 5.0$, and $k_C = 0.18$.

2.2. *Time series of spiking, bursting, and chaos based on the Ca^{2+}-activated K^+ channel model*

The dynamic nature of the model can be investigated by solving the three simultaneous differential equations [Eqs. (2.1, 2.2, and 2.3)] with a Gear algorithm. Figure 4 reveals interesting patterns that the model generates as g_p (the maximal conductance of the slow K^+ current) is increased. As shown here, when g_p is small the model gives rise to repetitive spiking (see the top trace). As g_p is increased, a period doubling sequence appears (the second trace), which leads to spiking-chaos (third trace) and then bursting-chaos (fourth trace). Bursting-chaos differs from spiking-chaos in that in the former an unpredictable number of spikes rides on the slow wave while in the latter there is no clear underlying slow wave. When g_p is increased to 14.098 there arises another type of bursting-chaos (see the fifth trace), whose structure is somewhat different from bursting chaos of the fourth frame. Note that the bursts shown in this trace consist mainly of three spikes that are followed by a few extra spikes. When g_p is increased further, a one-spike burster appears, but beyond this g_p value no more oscillation occurs.

The dynamic series shown here were obtained on a VAX with single precision. Although double precision does not alter the bifurcation structure, the location of the chaotic regime may be shifted slightly. For example, chaos that appeared at 14.098 in single precision is moved to 14.097 in double precision. This rich nonlinear dynamic behavior can be more fully elucidated by performing a bifurcation analysis as discussed below.

2.3. *Bifurcation analysis using AUTO*

How bifurcations and chaos arise from this model can be seen through a bifurcation diagram constructed using AUTO. Such a diagram is shown in Fig. 5, where the ordinate consists of a dependent dynamic variable (V), and the abscissa consists of a parameter that controls the pacemaker current, g_p. In the top frame, the steady state branch is represented by the purple line, and the periodic states by the red and green. Both red and green lines trace the maximum and minimum of membrane potential. In addition to giving the bifurcation diagram, AUTO also gives the period of the oscillation as a function of g_p, and this is shown by the bottom frame. As shown in this figure, there are two Hopf bifurcation points: the left Hopf bifurcation (LHB) at $g_p = -7.776$ and the right Hopf bifurcation (RHB) at $g_p = 26.853$. In the RHB, an unstable low amplitude periodic state develops which extends to $g_p = 26.855$ (see the inset). This

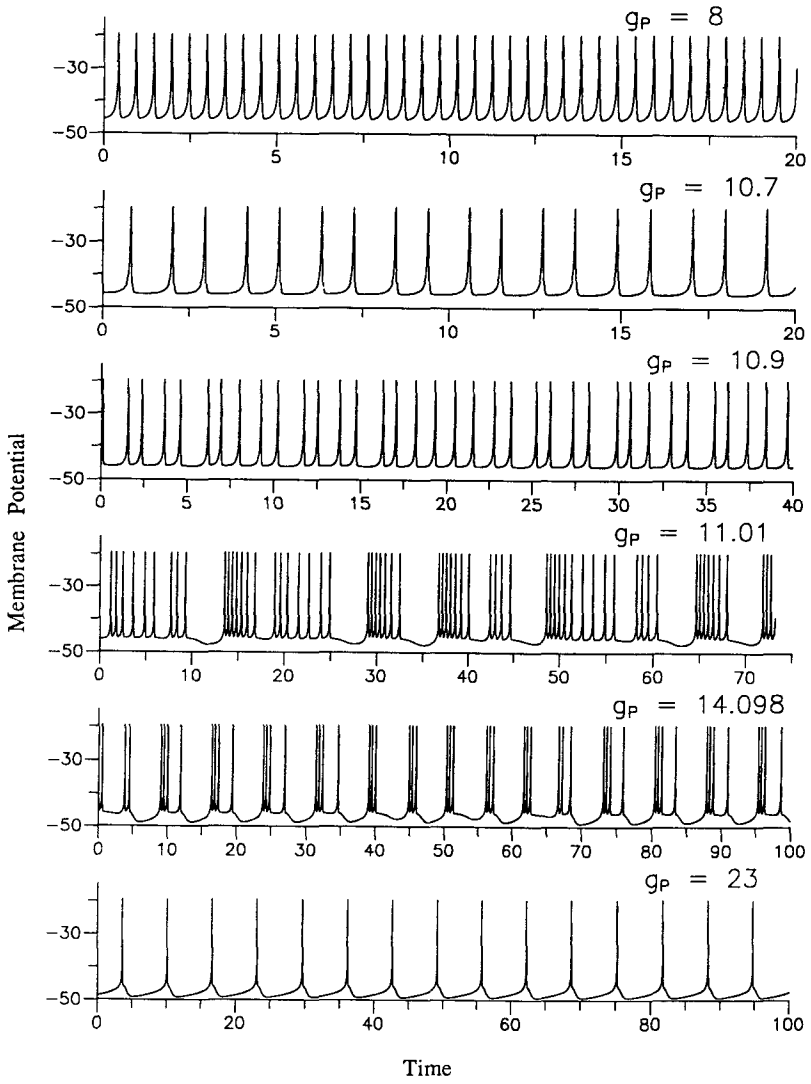

Fig. 4. Time series of the membrane potential, V, of the excitable cell based on the K–Ca channel hypothesis. (i) Repetitive spiking, (ii) period of two, (iii) spiking-chaos, (iv) bursting chaos, (v) chaos in the bifurcation regime where three spikes split into four spikes, and (vi) singlet bursting. The maximal conductance, g_p, of the K–Ca channel is listed in each trace.

point is known as the periodic limit point (PLP), and this type of Hopf bifurcation point is named as a subcritical Hopf bifurcation. From the PLP, the amplitude grows suddenly, and the periodic branch becomes stable. As one can see from the inset, between the RHB and PLP three states coexist; (i) a low-amplitude unstable oscillatory state, (ii) a high-amplitude stable periodic state, and (iii) a stable repolarized steady state.

Note that there are two periodic branches — the green branch which evolves from the LHB and terminates at $g_p = 19.243$ with an infinite period, and the red branch which evolves from the RHB and terminates when it meets the green branch at 10.6359. The red branch is a "spiking" branch, in that the mode of oscillation in this branch consists mainly repetitive spiking. On the other hand, the green branch is a "bursting" branch, where the bursting presides in this branch. In the region between $g_p = 10.6359$ and 19.243, the bursting branch (red) and the spiking branch (green) coexist, where the red branch is a stable one and the green branch is an unstable one. In the neighborhood of the intersection of the two branches (i.e., 10.6359), however, both modes of oscillations become almost equally stable. This convergence of two modes of oscillation gives rise to doublets of spikes. Indeed, the time series of V shows that a period doubling sequence starts from this intersection (see the second trace of Fig. 4), which transforms to chaos

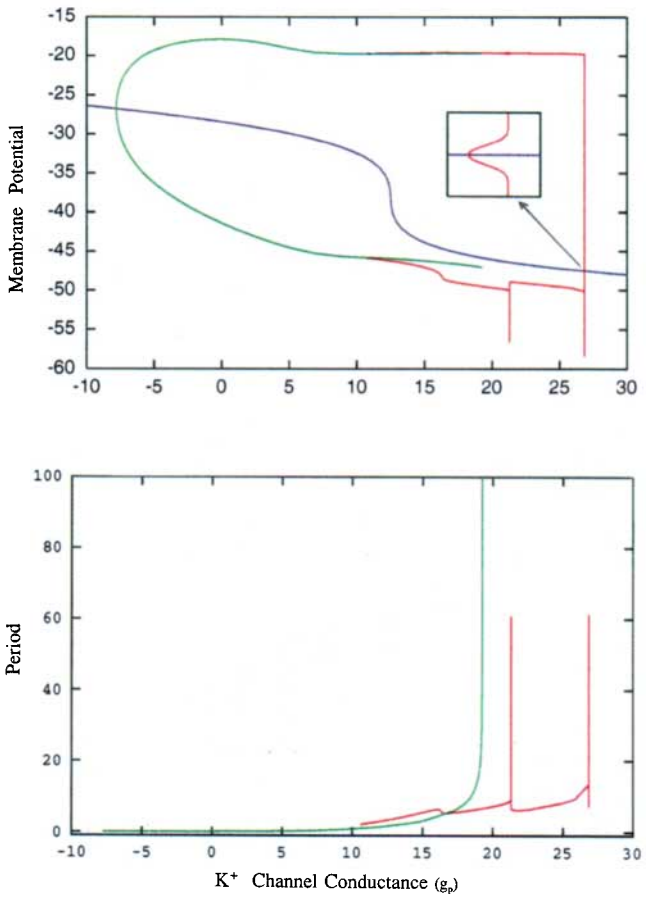

Fig. 5. Bifurcation diagram constructed using AUTO for the model that is based on the K–Ca channel. The upper frame shows the maximum and minimum of membrane potential V as a function of g_p (the maximal conductance of the slow outward current), and the lower frame shows the periods of oscillations in the periodic branches shown in the upper frame. Here, the purple line is a steady-state branch, the red line is a bursting branch, and the green line is a spiking branch. The inset shows the neighborhood of the right Hopf bifurcation, where the stable period, unstable period, and repolarized resting state coexist.

(see the third and fourth traces) as g_p increases. In other words, *this bifurcation diagram predicts that a periodic doubling sequence will be initiated when two modes of oscillations converge at one point* (*i.e.*, $g_p = 10.6359$).

In addition to predicting the regime of periodic-doubling, AUTO also predicts three bifurcation points where an n-spike burst transforms to an n+1-spike burst. The first bifurcation point is located at $g_p = 26.85$, where a stable one-spike burst arises from a low-amplitude unstable oscillation (see the bottom trace of Fig. 4 for illustration). The second bifurcation is located at $g_p = 21.315$ where a one-spike burst becomes a two-spike burst. There is another bifurcation point at $g_p = 16.39$; at this bifurcation a two-spike burst becomes a three-spike burst. At each of the first two bifurcation points, a stable periodic state is connected to an unstable periodic branch where the period of the burst becomes very large and the minimum of the membrane potential becomes very low.

2.4. *Bifurcation diagram in the region of complex dynamics*

In the region where two periodic states coexist (i.e., $10.6359 < g_p < 19.243$), there may exist several other unstable periodic branches. A detailed bifurcation structure can be seen more clearly through the bifurcation diagram shown in Fig. 6. Here, frame (a) reveals the spike-to-spike interval plotted as a function of g_p, frame (b) reveals the probability of opening of the Ca^{2+}-sensitive K^+ channel (expressed by p) plotted as an increasing function of g_p, and frame (c) is a blow-up of the region where the doublets transform to bursting via chaos. These plots were obtained by solving the three simultaneous equations [cf. Eqs. (2.1)–(2.3)] for a given g_p, where g_p is increased incrementally by a small step starting from the LHB and ending at the RHB. The spike-to-spike intervals [in frame (a)] were obtained by (i) recording the time, $\tau(n)$, when the upstroke of the nth spike crosses the $V = -45$ mV line and (ii) subtracting $\tau(n)$ from $\tau(n-1)$. The values of p [in frames (b) and (c)] are those values that p takes when the upstroke of V crosses the $V = -30$ mV line. To ensure that the limit cycle values are included, we threw away the first few hundred cycles.

Note in this figure that as g_p is increased (i.e., as the system moves from the depolarized state to the repolarized state), there arises a very complex dynamic regime (hereafter we refer to this region as complex-1). First, the spike splits into doublets at $g_p = 10.64$, and the two spikes split into quadruplets at $g_p = 10.81$. This periodic doubling scenario leads to spiking-chaos as g_p is increased [see frame (c)]. Spiking-chaos exists between $10.87 < g_p < 10.98$, and the time series of this sequence can be seen in the second trace of Fig. 4. Within this regime, there exists an infinite number of chaotic attractors. Around $g_p = 10.93$, however, three nonchaotic attractors appear within chaotic attractors, i.e., this model *exhibits subduction* according to the definition of Grebogi & Ott [1983]. On the left side of the subduction, the characteristic behavior of chaos

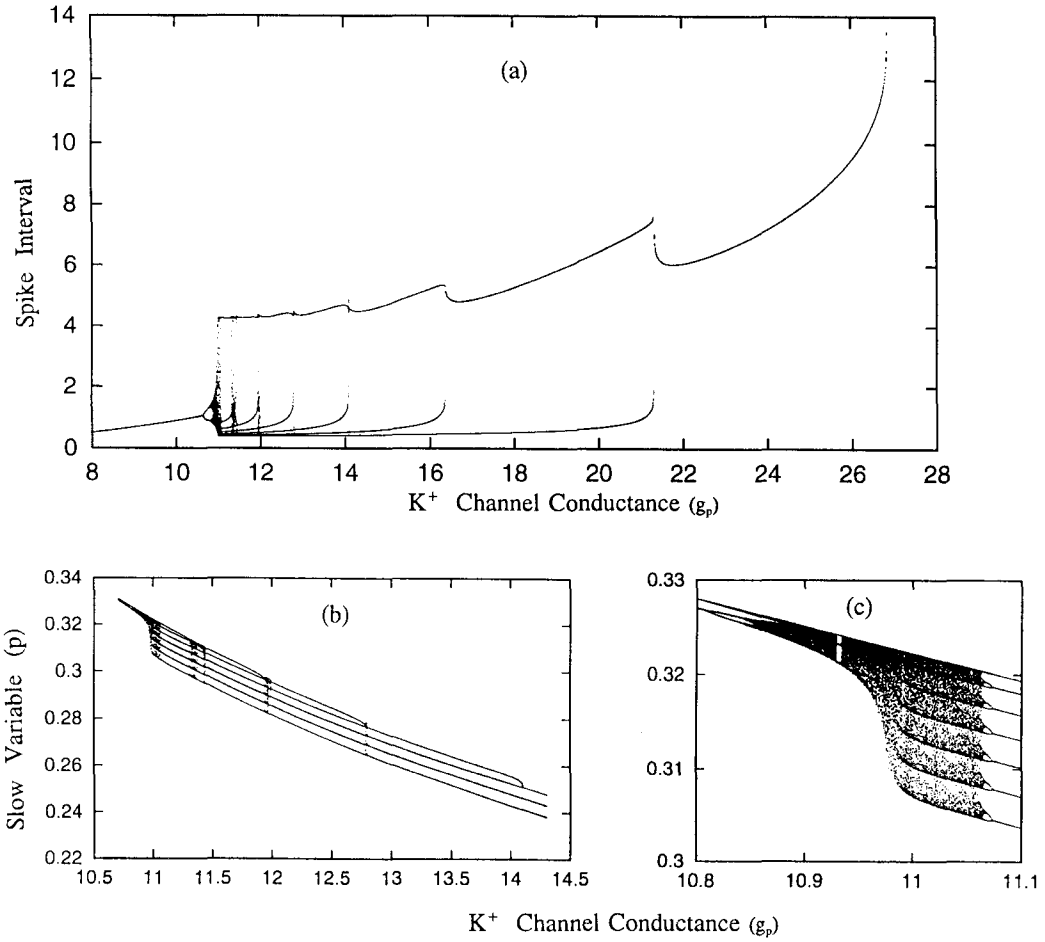

Fig. 6. Bifurcation diagram constructed by solving three simultaneous differential equations in Sec. 2.1. Frame (a) shows the spike-to-spike interval, i.e., the time interval taken by two consecutive spikes (recorded whenever the upstroke of spikes crosses the line $V = -45$ mV) plotted against g_p (the maximal conductance of a slow outward current). Frame (b) shows p, the probability of opening of K–Ca channel as a function of g_p. The p values are picked whenever the upstroke of spikes crosses the line $V = -30$ mV. Frame (c) shows the complex oscillatory regime that appears in the depolarized phase. Here, p can be viewed as the fraction of the available K–Ca channels at time t.

is intermittence. The intermittent chaos occurs via tangent bifurcation [Grebogi & Ott, 1983]. On the right side of it, another periodic doubling scenario starts from each of the three branches. This period doubling sequence has a self-similar structure with the original period-doubling scenario.

As the system moves to the right, the bifurcation structure suddenly enlarges with a small change in g_p, and spiking-chaos transforms to the bursting-chaos. This transition may be classified as an *interior crisis* according to the definition of Grebogi & Ott [1983]. After the occurrence of the interior crisis, certain characteristic statistical behaviors occur. Points are condensed to seven bands of attractors, in which the lower bounds seem to be more condensed than the upper ones, i.e., the lower branches are more attractive than the upper ones. The significance of the seven bands can be realized in the time series of bursting chaos (see the fourth trace of Fig. 4), where the seven consecutive spikes appear more often than others. The interior crisis observed here is a new type of crisis in that *spiking-chaos (without any apparent interior structure) transforms to bursting-chaos which contain several (odd number) bands of attractors.* The transition from spiking-chaos to bursting-chaos was observed previously in excitable models by Chay [1984, 1985, 1986], Chay & Kang [1987], Chay & Lee [1990], and Chay & Rinzel [1985]. The characteristics of the crisis transition have been studied by Holden & Fan [1992a,b,c] and Fan & Holden [1993] using the Hindmarsh & Rose model [1983] and also by Fan & Chay [1993, 1994a–c] using the Chay model [1985]. A refined analysis has also been

carried out by Kaas–Petersen [1987] using both the Hindmarsh–Rose and Chay models.

As the system leaves the bursting-chaotic regime, an inverse period doubling sequence appears around $g_p = 11.065$, in which the underlying slow wave now starts to double. The period of two is the only clear sequence one can find in this regime (i.e., $11.065 < g_p < 11.071$). This period of two differs from the period-2 in the period-doubling scenario seen earlier, in that the former consists of two types of bursting (each burst contains seven spikes but the underlying waves have two different shapes) whereas the latter consists of doublets of spikes. Then, the period of two transforms to a period of one where the slow wave comes only in one shape. Beyond this doubling sequence (i.e., around $g_p = 11.4$) a periodic bursting with seven spikes (i.e., we call this seven-spike bursting) appears first. This then transforms to a six-spike bursting around $g_p = 11.3$. As the system moves further to the right from the six-spike bursting regime, the number of spikes decreases one by one — from six spikes to five at $g_p = 11.94$, from five to four at $g_p = 12.81$, from four to three at $g_p = 14.13$, from three spikes to two spikes $g_p = 16.38$, and from two spikes to one at $g_p = 21.31$. Finally a threshold unstable oscillation appears at $g_p = 26.855$.

2.5. *Complex structure embedded in the spike reducing bifurcating zone*

How the spikes split one by one at the bifurcating zone is an interesting phenomenon. Figure 7 depicts the first four bifurcating zones that appear as the system moves away from the seven-spike bursting regime toward the one-spiking bursting regime. As g_p increases, a complex structure shown in frame (d) appears first that is followed by the structure shown in frame (c), then a less complex structure in frame (b), and finally a simpler structure in frame (a).

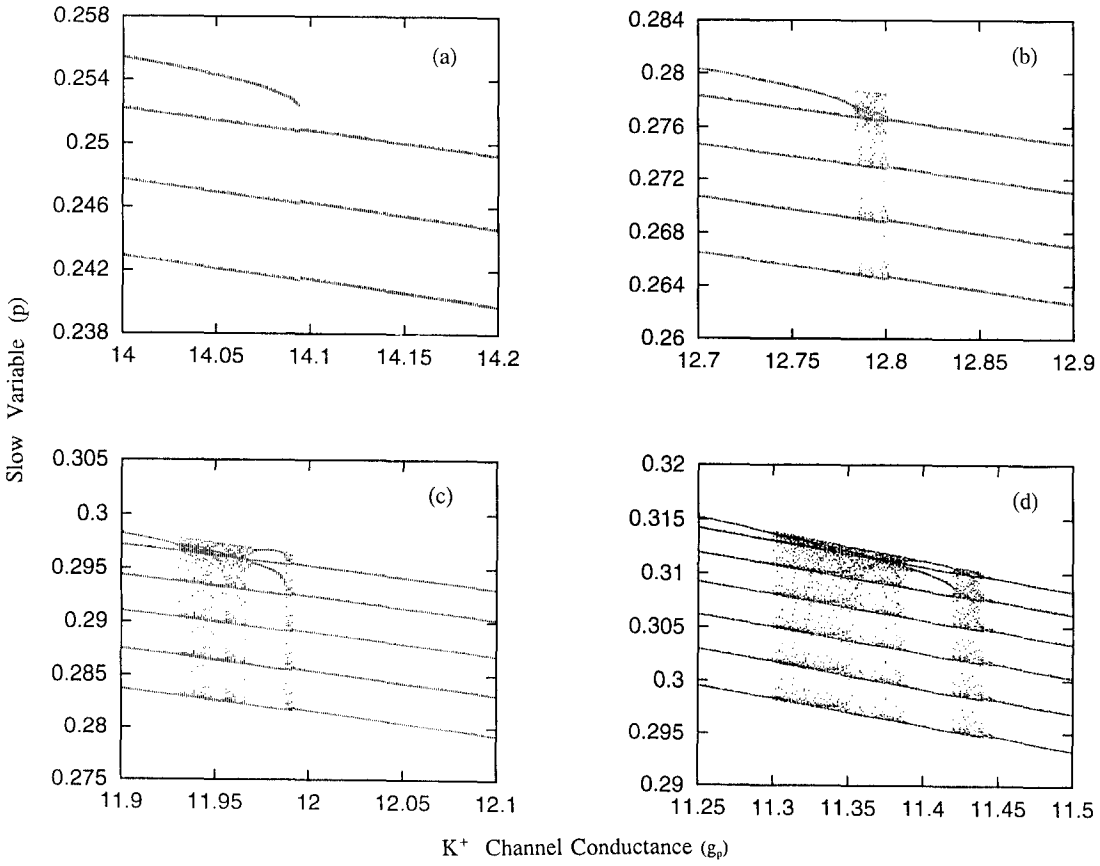

Fig. 7. Enlarged portions of the transition zones, where four spikes are decreased to three [frame (a)], five spikes are decreased to four [frame (b)], six spikes are decreased to five [frame (c)], and seven spikes are decreased to six [frame (d)], as the system moves from the depolarized phase to the repolarized phase.

In frame (a), we see that four spikes are reduced to three spikes, and in frame (b) five spikes are reduced to four spikes. In frame (c), six spikes are reduced to five spikes, and finally seven spikes are reduced to six spikes [frame (d)]. Note that *the dynamic structure becomes more and more complex as the number of spikes increases.* Note also that the range of the transition zone becomes increasingly wider as the number of spikes increases.

It is easier to start out our discussion with the simplest structure, which is the structure in frame (a). That is, we start out our discussion from the repolarized region and move to the depolarized region. As g_p increases, the top attractive branch in frame (a) dives toward the second branch. As it gets closer to the second branch, chaos ($C1$) arises; this chaos is hardly visible here. In fact, the range where $C1$ resides is so narrow that its existence can only be seen through the dynamic solution. See the fifth trace in Fig. 4. In this trace, the bursting in $C1$ consists mostly of three spikes. These three spikes came from those three attractors that appear in frame (a).

A structure similar to frame (a) also appears in frame (b); however, the range of the chaotic regime ($C1$) is much wider than that in frame (a). In this regime the bursting consists mostly of four-spike bursting separated by a few extra spikes in a very erratic manner. Chaos that exists in $C1$ is classified as semichaos [Fan & Chay, 1994b]. We call this semichaos since although this is true chaos there are four clear lines at which these four chaotic attractors are visited more often than is any other attractor lying in $C1$. The top attractor is the least attractive one, whereas the bottom attractor is the most attractive one. In the case of traditional chaos, the chaotic attractors lie anywhere between the upper and lower bounds of $C1$.

A dynamic structure similar to frame *b* appears in the transition zone between the six-spike bursting and five-spike bursting (see frame *c*). However, there appears one more chaotic regime ($C2$) on the right. As the system moves from the left to the right (i.e., as g_p increases), the top branch gets closer to the second branch, and this induces $C1$. Note that $C1$ has a more complex pattern and its range is wider than that of frame (b). As the system leaves $C1$, there appear five "basic" branches (which came from the bottom five branches) and two extra branches (upper and lower) which bifurcated from the top band of chaotic attractors. These seven attractors induce "seven-spike" bursting ($R1$). This burster differs from the normal seven-spike burster [in frame (d)] in that the first five consecutive spikes in this burster are separated from the remaining two by a pause. The last two spikes in this "seven-spike" bursting came from the two extra branches that are bifurcated from $C1$. In the case of normal seven-spike bursting, the interval between the spikes increases gradually without any pause between them. As the system moves more to the right, the upper extra branch gets closer to the first basic branch, while the lower branch gets closer to the second basic branch. This merger gives rise to $C2$. After passing $C2$, normal six-spike bursting appears.

The dynamic structure in frame (d) is very similar to that in frame (c), except that the ranges in which $C1$ and $C2$ reside are wider. On the left of $C1$ resides the normal seven-spike bursting. Burstings in $C1$ and $C2$ consist mostly of seven- and six-spikes, respectively, separated by a few extra spikes in an erratic manner. The $R1$ regime resides between $g_p = 11.39$ and 11.43, and "eight-spike" bursting exists here. As the system leaves $C2$, an inverse period doubling sequence appears beyond $g_p = 11.4485$ which lasts to $g_p = 11.4488$. The doublets which exist in this range consists of two types of slow waves (one whose minimum potential is lower than the other). Each of the doublets consists of six spikes. Then, this inverse period-doubling sequence terminates when the doublets in the slow wave transform to singlets, giving rise to normal six-spike bursting.

2.6. *Lyapunov exponents*

The Lyapunov exponents are good measures with which to find whether chaos generated by the model is truly deterministic or quasiperiodic in nature. In Fig. 8, the largest Lyapunov exponent λ_1 (the solid curve) and the next largest exponent λ_2 (the dash-and-dot) are displayed as a function of g_p. The upper inset shows the smallest Lyapunov exponent λ_3 as a function of g_p, and the lower inset shows the first four complex regimes that exist in this model in an expanded scale. In order to obtain these exponents, the three differential equations in the model were solved using a two-time step Euler method with a fixed time increment (Δt ranging from 2×10^{-5} to 1×10^{-5}) and with a maximum time equal to 500. To shorten our computation time, we utilized a look-up table where all the exponential terms (see Appendix I) were computed as a

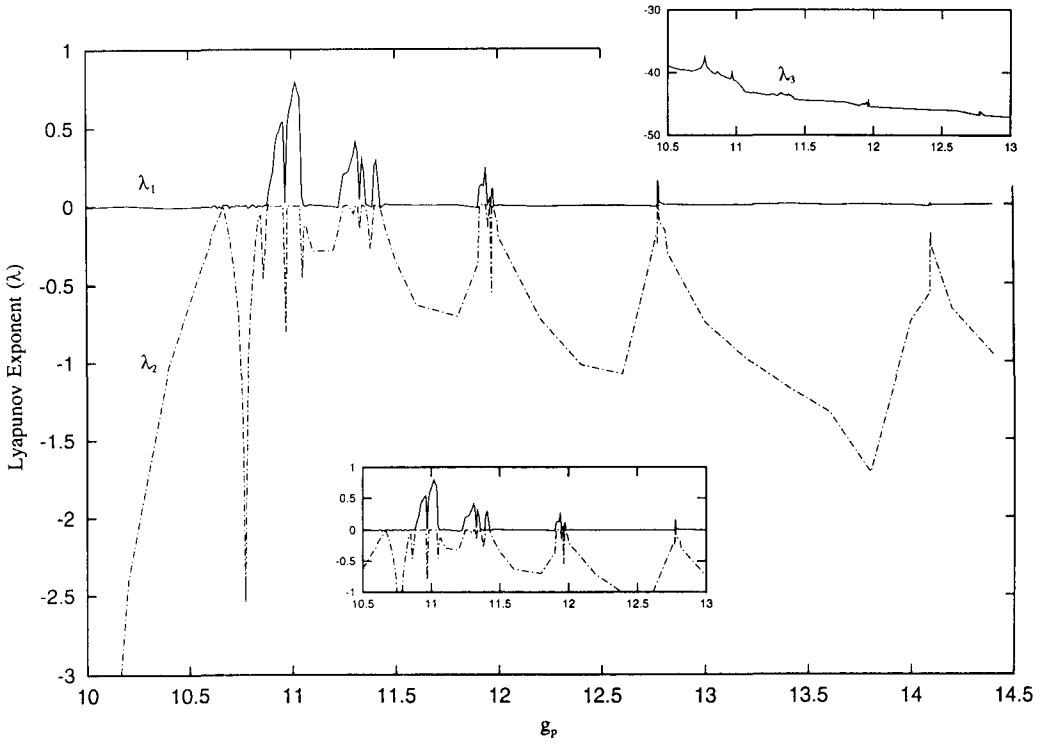

Fig. 8. The first two Lyapunov exponents as a function of g_p, which reveal the chaotic regimes and the bifurcating regions where the n spikes split to $n + 1$. Here, the solid and dash–dot lines are, respectively, the largest and next largest Lyapunov exponents. The upper inset shows the smallest Lyapunov exponent as a function of g_p. The lower inset shows the first two exponents in an expanded scale.

function of V at the beginning of the program, placed them in a tabular form, and read them whenever needed. The three Lyapunov exponents λ_1, λ_2, and λ_3 were computed using the method of Wolf *et al.* [1985] for a fixed g_p. We then increased g_p incrementally and automatically starting from the repetitive spiking regime. The exponents shown in this figure were obtained by summing all of λ_i ($i = 1, 2, 3$) values from $t = 450$ to $t = 500$ and dividing it by $500/\Delta t$, i.e., they are the means of λ_i for the last 500 seconds.

Note that λ_1 becomes positive and λ_2 becomes zero in the chaotic regime. At each bifurcation point, both exponents become zero. The fact that λ_1 became positive in the complex regimes verifies that the chaos that appears in these regimes is truly deterministic chaos. In the complex-5 regime, however, our increment was too coarse to locate the chaotic regime there. It is interesting to note that the Lyapunov exponents can provide information on many of the complex structures that exist in the model. That is, they can locate the periodic doubling regime, the periodic regime (i.e., period-3) in the complex-1, the regular periods that are embedded in the complex-2 and complex-3 regimes (in addition to the chaotic regimes). Among all these interesting features that the Lyapunov exponents can provide, the most interesting feature is the magnitude of λ_1 in the chaotic regimes. Note that the most irregular region is the bursting-chaotic regime (i.e., $10.82 < g_p < 11.07$), so λ_1 is largest there. On the other hand, the complex-5 regime ($g_p = 14.10$) is least complex, so λ_1 is smallest there. Thus, *the magnitude of the largest Lyapunov exponent can be used as a measure for the degree of complexity (i.e., the degree of irregularity) of deterministic chaos.*

2.7. *Why spiking, bursting and chaos?*

Although the bifurcation diagrams presented in Figs. 5 and 6 reveal the types of complex structures, these diagrams tell little about why such structures are induced when the bifurcation parameter varies. How spiking, bursting, and chaos arise from this

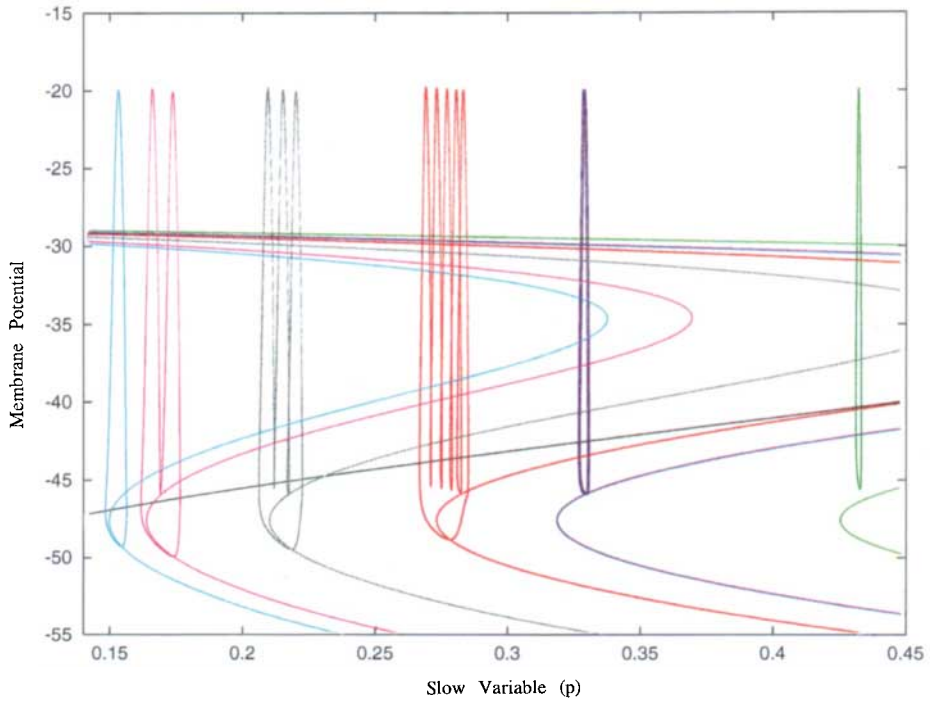

Fig. 9. The dynamic orbits projected on the V–p phase plane and their respective V-nullclines (dV/dt). Here, the black curve is the p-nullcline ($dp/dt = 0$), the z-shaped curves and the spikes are respectively the V-nullclines and the dynamic orbits at various values of g_p: $g_p = 8$ (green), $g_p = 10.7$ (purple), $g_p = 12.5$ (red), $g_p = 16.3$ (gray), $g_p = 21.0$ (pink), and $g_p = 23.0$ (blue).

model can be explained by studying how the dynamic orbit travels on the V–p phase plane relative to the V-nullcline ($dV/dt = 0$) and the p-nullcline ($dp/dt = 0$). This type of dynamic orbital study was first carried out by Rinzel & Lee [1986, 1987] using both the neuronal model of Plant [1981] and pancreatic β-cell model of Chay-Keizer [1983] and Lee *et al.* [1983].

Figure 9 reveals those orbits traveled by a spike at five different locations of the bifurcation diagrams in Fig. 5. On this plane we have superimposed two nullclines, where the black line is the p-nullcline and the z-shaped curves are the V-nullclines at the corresponding five g_p values. Here, the green trajectory ($g_p = 8$) reveals repetitive spiking; the purple trajectory ($g_p = 10.7$) doublets; the red trajectory ($g_p = 12.5$) a five-spike burster; the gray trajectory ($g_p = 16.3$) a three-spike burster, the pink trajectory ($g_p = 21.0$) a two-spike burster, and the blue trajectory ($g_p = 23.0$) a one-spike burster. Note that the p-nullcline is invariant to g_p, while the V-nullcline slides to the left as g_p increases. In the V-nullcline, the two ends of the curved portion of the letter z are termed the "knees." So, there are three branches that the orbit has to cross — the upper unstable branch (hereafter referred to as the Z_1 branch), the middle curved branch (Z_2), and the lower stable branch (Z_3).

To proceed with our discussion, it is important to note the location of the homoclinic point relative to that of the steady state point. The homoclinic point (HCP) is the point where the stable periodic branch intersects the Z_2 branch. At the homoclinic point, the period becomes infinity. The spiking terminates as soon as it passes the HCP. Thus, the farther the HCP is from the knee the more spikings can be accommodated. The steady state point (SSP) is the intersection between the two nullclines. If the spike falls into the SSP, it will stay there for a long time. Both the SSP and the HCP lie on the Z_2 branch, where the SSP can be located in this figure but the HCP can be visualized only as a point very near to the termination of the final spike. Note that for the one-spike burster (blue) and the two-spike burster (pink) the HCP is located on the right side of SSP, while for the others it is located on the left side of the SSP. When HCP is located on the left of the SSP, a spike traveling upward makes a spiral form (i.e., to the left, up, and right) before entering the Z_1 branch. Because of this spiral movement,

the spike width becomes narrower. The narrowness of the spike width makes the spike approach closer to the HCP.

Why does repetitive spiking arise when g_p is small? Take for example the green spike on the right side. Here, the upstroke of the spike is caused by the inward current, and the downstroke is caused by the K^+ currents. Consider the spike at its maximum potential. At this point dV/dt is negative, so the direction of the spike is downward. The spike which travels in the downward direction will first pass the Z_1 branch and then the p-nullcline. As the spike passes the Z_1 branch, it experiences an upward pull (since dV/dt becomes positive below this line), at first a weak pull but later a strong pull. After passing the p-nullcline, the spike is pulled to the left (since dp/dt becomes negative). The K^+ current is too weak to pull the spike further downward, so the spike reverses its path without reaching the Z_2 branch. As the spike moves upward and passes the Z_1 branch, it is pulled downward again. The cycle repeats. Thus, repetitive spiking results when the trajectory does not have enough downward pull to reach the Z_2. The path that the spike takes is clockwise. The doublets (see the purple trajectory) result when two spikes are closely spaced, and the second spike almost touches the Z_2 branch. This can be better understood from Fig. 5 where the bursting periodic branch (red) touches the spiking periodic branch (green) at around $g_p = 10.6$. This makes the green branch almost as stable as the red branch.

Regular bursting shown on the left in Fig. 9 can be explained as follows. Take the case of the red burster in the middle. Let the spike travel on the Z_3 branch (i.e., the repolarized phase) first. Along this branch dp/dt is negative, so the spike travels from the right to the left. As the spike passes the knee of the V-nullcline, it will be pulled upward (since $dV/dt > 0$), then pass the p-nullcline (the black line), and then the Z_1 branch. As it passes the Z_1 branch, the spike experiences a downward pull (now dV/dt is less than zero). So, the spike will reverse its path and travel downward passing the p-nullcline. As it passes the p-nullcline, the spike will experience a strong left- and up-ward pull again (since $dp/dt < 0$ and $dV/dt > 0$), and this will initiate the next spike. As the spike traveling upward re-crosses the p-nullcline, the spike will experience a pull toward the right (since $dp/dt > 0$). The spike continues to travel upward (since dV/dt is still positive here), but its position is shifted to the right (making a spiral form). The spiking will continue four more times, but each time the minimum of the spike becomes more repolarized. On the fifth time downward, the spike touches Z_2 branch. As it touches the Z_2 branch, the spike experiences a strong downward pull (since beyond this point $dV/dt < 0$) and lands on the Z_3 branch. This is how the bursting occurs.

How would the spike split one by one as g_p decreases? When g_p is very large (e.g., the blue orbit), both the HCP and the SSP are located close to the knee and the SSP is located to the left of the HCP. This makes the width of the spike very broad. Because the HCP is so close to the knee, only one (big) spike can be accommodated. As g_p decreases, the HCP moves farther away from the knee, but the SSP moves even farther than the HCP. The first movement makes more spikings possible, and the latter movement makes the spike width narrower. The movement of HCP and the narrowness of the spike width make additional spiking possible. Spike splitting stops when the spike no longer can reach the Z_2 branch.

Chaos that appears on the boundary between the n-spike bursting and the $n+1$-spike bursting can be explained by the following mechanism. Near the bifurcating point where n spikes split into $n+1$ spikes, the nth spike approaches very close to the HCP. As the nth spike gets closer to the HCP (i.e., "black hole"), there exists an infinite number of periods for given V and p. In fact, AUTO predicts that p and V fluctuate many times while approaching the homoclinic orbit (i.e., there exist multiperiodicities for given V and p). The existence of multiperiodicity in the neighborhood of the HCP means that an infinitesimal change in V would make the timing of the next spike impossible to predict, i.e., chaos sets in. In other words, *chaos results when the spike approaches very, very close to the homoclinic orbit, where it takes a variable length of time for the spike to come out of the black hole.* The complex structure disappears as the system passes this transition zone because both the SSP and the HCP move to other locations (due to the change in g_p).

This also explains why the complex regime does not exist in the transition zone between the one- and two-spike burstings and also between the two- and three-spike burstings. When g_p is large, the SSP is located to the left of the HCP and the spike width is quite broad. Since the spike width is broad, the spike cannot get closer to the homoclinic point, i.e.,

there is little chance that the spike can fall into the black hole. This also explains why the complex structure becomes more and more complex (and complex-1 is most complex of all) as g_p becomes smaller. This is because as the system moves toward the depolarized state, the spike width becomes narrower. The narrowness allows the spike to get increasingly closer to the HCP.

2.8. *Model based on a Ca^{2+} blockable Ca^{2+} channel*

The model presented in this section is based on the Ca^{2+}-blockable Ca^{2+} channel presented in Chay [1990c], Chay & Lee [1990], and Chay & Fan [1993]. This model contains four ionic currents — the fast inward current I_{fast}, the slow Ca^{2+} current I_{slow}, the delayed rectifying K^+ current I_K, and the leak current I_{leak}. There are six dynamic variables in this model. The first variable is membrane potential V which changes with time in the following form:

$$-C_m\frac{dV}{dt}=g_{\text{fast}}m_\infty h(V-V_{\text{fast}})+g_{\text{slow}}df(V-V_{\text{slow}}) +g_K n(V-V_K)+g_L(V-V_L) \qquad (2.4)$$

where g_{fast}, g_{slow}, g_K, and g_L are the maximal conductances of a fast inward current, a slow calcium current, a delayed rectifying K^+ current, and a leak current; V_{fast}, V_{slow}, V_K, and V_L are the reversal potentials for their respective currents; m and h are the activation and inactivation gating variables of the fast current (where m_∞ is the m at the steady state), d and f are the activation and inactivation of the slow inward current, and n is the opening probability of the outward current. Note that Eq. (2.4) also contains four types of currents as in Eq. (2.1). In this model, the second term is responsible for the genesis of the slow underlying wave, whereas in the first model the third term is responsible for this wave.

The hypothesis in this model is that the Ca^{2+} channel becomes inactive when a Ca^{2+} ion binds to the receptor site located at the pore of the channel. Accordingly, its kinetic scheme may be represented as follows:

$$\text{BLOCKED} \underset{\lambda_f C}{\overset{\lambda_f}{\rightleftharpoons}} \text{UNBLOCKED} \qquad (2.5)$$

where $C = [Ca^{2+}]_i/K_{\text{Ca}}$, λ_f is the forward kinetic constant from the blocked state to the unblocked state, and K_{Ca} is the dissociation constant of the Ca^{2+} ion from its receptor site located in the pore of the Ca^{2+} channel. Then, the fraction of calcium channels which is unblocked, f, can be obtained from the above kinetic scheme as,

$$\frac{df}{dt}=\lambda_f(1-f)-\lambda_f\frac{[Ca^{2+}]_i}{K_{\text{Ca}}}f. \qquad (2.6)$$

In the modern view, f can be interpreted as the fraction of available Ca^{2+} channels at time t (instead of the inactivation variable). As $[Ca^{2+}]_i$ increases, the availability of functional Ca^{2+} channels decreases due to dephosphorylation by a calcium-dependent protein [Armstrong, 1989]. If the process described in Eq. (2.5) is fast (i.e., λ_f is large) then f can be approximated by its steady state value $f_\infty = 1/(1+C)$. This is the expression used by others to describe the inactivation term of the Ca^{2+} channel (Chad and Eckert, 1986), but as we show here it has a limited applicability.

As in the Hodgkin–Huxley model [1952], we assume that the three other gating variables h, d, n depend on time and potential in such a way that

$$\frac{dy}{dt}=\frac{y_\infty-y}{\tau_y}, \quad y=h,\ d,\ \text{and}\ n, \qquad (2.7)$$

where y_∞ and τ_y are the y at its steady state and relaxation constant, respectively. Here, the steady state expression takes the following form,

$$y_\infty=\frac{1}{1+\exp\left(\dfrac{V_y-V}{S_y}\right)}, \quad y=m,\ h,\ d,\ \text{and}\ n.$$

According to this model, the relaxation constants take the form

$$\tau_y=\frac{\tau_y^*}{1+\exp\left(a_y\dfrac{V_y-V}{S_y}\right)+\exp\left((a_y-1)\dfrac{V_y-V}{S_y}\right)},$$
$$y=h,\ d,\ \text{and}\ n,$$

where V_y is the voltage at the half maximal point, S_y is the slope at $V=V_y$, τ_y^* is the maximal relaxation time constant, and a_y determines how the relaxation constant τ_y depends on voltage (for example, $a_y=0.5$ makes τ_y a bell shape as an increasing function of V).

In the scheme shown by Eq. (2.5), $[Ca^{2+}]_i$ depends on the influx of Ca^{2+} from outside through the calcium channel and the efflux of Ca^{2+} via the

Ca^{2+}-pump. This effect is expressed by the following mathematical expression:

$$\frac{dC}{dt} = \rho\left\{\frac{g_{\text{slow}} df(V_{\text{slow}} - V)}{\sigma} - k_{\text{Ca}}C + k_{\text{Ca}}C_r\right\},$$

$$C = \frac{[Ca^{2+}]_i}{K_{\text{Ca}}}, \tag{2.8}$$

where ρ is a measure of the Ca^{2+} buffer capacity of the cell, and σ is a factor that converts the electromotive force to the concentration gradient multiplied by K_{Ca}. In the above expression, C_r is equal to $[Ca^{2+}]_r/K_{\text{Ca}}$, where $[Ca^{2+}]_r$ is the intracellular calcium concentration at the resting potential. Note here that if ρ is large, one can introduce a rapid equilibrium assumption such that C can be expressed by

$$C = C_r + \frac{g_{\text{slow}} df(V_{\text{slow}} - V)}{k_{\text{Ca}}\sigma}.$$

This relation would approximately hold for ρ greater than 10, and thus for $\rho > 10$ the six dynamic variables in the model can be reduced to five.

To reiterate, in this model the slow Ca^{2+} current is responsible for the slow wave that underlies the bursting, and the fast inward current together with the delayed rectifying K^+ current is responsible for generating the spike activity. There are altogether six dynamic variables, V [Eq. (2.4)], h [Eq. (2.7)], d [Eq. (2.7)], f [Eq. (2.6)], n [Eq. (2.7)], and $[Ca^{2+}]_i$ [Eq. (2.8)]. In this model, λ_f determines the burst periodicity, i.e., the smaller the value of λ_f, the longer the burst periodicity becomes. However, as shown in Eq. (2.5) (since the rate of closing is determined by $[Ca^{2+}]_i$) ρ also determines the burst periodicity, i.e., the smaller the value of ρ, the longer the burst periodicity becomes. The parametric values that define the model are: $C_m = 1$, $g_{\text{fast}} = 1000$, $g_{\text{slow}} = 18$, $g_K = 200$, $g_L = 10$, $V_{\text{fast}} = 60$, $V_{\text{slow}} = 140$, $V_K = -80$, $V_L = -60$, $V_m = -12$, $S_m = 5$, $V_h = -40$, $S_h = -6$, $V_d = -30$, $S_d = 10$, $V_n = 15$, $S_n = 15$, $\tau_h* = 0.1$, $\tau_d* = 0.5$, $\tau_n* = 0.1$, $\lambda_f = 0.01$, $\sigma = 193$, $\rho = 20$, $C_r = 0.1$, $k_{\text{Ca}} = 0.5$, $a_h = 0.5$, $a_d = 0.5$, $a_n = 0$, and $K_{\text{Ca}} = 0.7$.

There are alternative models based on other Ca^{2+} channel inactivation mechanisms in the literature. Some of these models are presented in Appendix III, especially in their reduced three-variable forms. All these models, although their forms are very different, give rise to interesting patterns of bursting and chaos. The patterns are similar to those observed in the previous sections when a certain parameter in the model, representing the availability of the key ion channel, is varied.

2.9. *Dynamic solution of the Ca^{2+}-blockable Ca^{2+} channel*

Figure 10 shows the time course of membrane potential V (solid lines) and $[Ca^{2+}]_i$ oscillation (dashed lines) predicted by the Ca^{2+}-blockable Ca^{2+} channel model. Note that the burst simulated from this model has an appearance very similar to those observed in neuronal bursting [Strumwasser, 1968; Junge & Stephens, 1973; Gorman *et al.*, 1982]. It differs from that of the first model in that the spikes undershoot the slow wave potential, while in the three-variable model treated above the spikes remain above the plateau potential. Note in this figure that the shape of the electrical burst is unaffected by the buffer strength ρ [see Eq. (2.8)]. However, as ρ decreases the burst period increases, and as the burst period increases the number of spikes increases. Although the shape of electrical bursting is not affected by ρ, the shape of $[Ca^{2+}]_i$ oscillations changes dramatically as ρ changes. If ρ is equal to 20, $[Ca^{2+}]_i$ oscillates in bursts in parallel to electrical bursting (see the top trace). If ρ is equal to one (see the middle trace), then the peak of $[Ca^{2+}]_i$ oscillation occurs shortly after the onset of electrical spike activity with spike activity being still visible (see the middle trace). If ρ is equal to 0.1, $[Ca^{2+}]_i$ oscillates out-of-phase with electrical bursting such that it peaks at a maximum near the termination of the plateau and reaches a minimum just before the onset of the active phase. During the active phase $[Ca^{2+}]_i$ gradually increases without spikes (see the bottom trace).

As shown in this figure, the period of a burst becomes large as ρ decreases. How ρ controls the burst periodicity can be understood from the kinetic scheme in Eq. (2.5). In this kinetic scheme, the period of the slow wave is determined by a parameter that affects the blocking and unblocking process of the Ca^{2+} channels. Note that the apparent rate of the blocking process is affected by the dynamic change of $[Ca^{2+}]_i$. This rate, in turn, is controlled by ρ which determines how fast $[Ca^{2+}]_i$ changes with varying membrane potential (see Fig. 10). Thus ρ is one of the factors that control the burst periodicity (via the rate of the change in $[Ca^{2+}]_i$). The plateau fraction (i.e., the duration of the period of spike activity divided by the burst

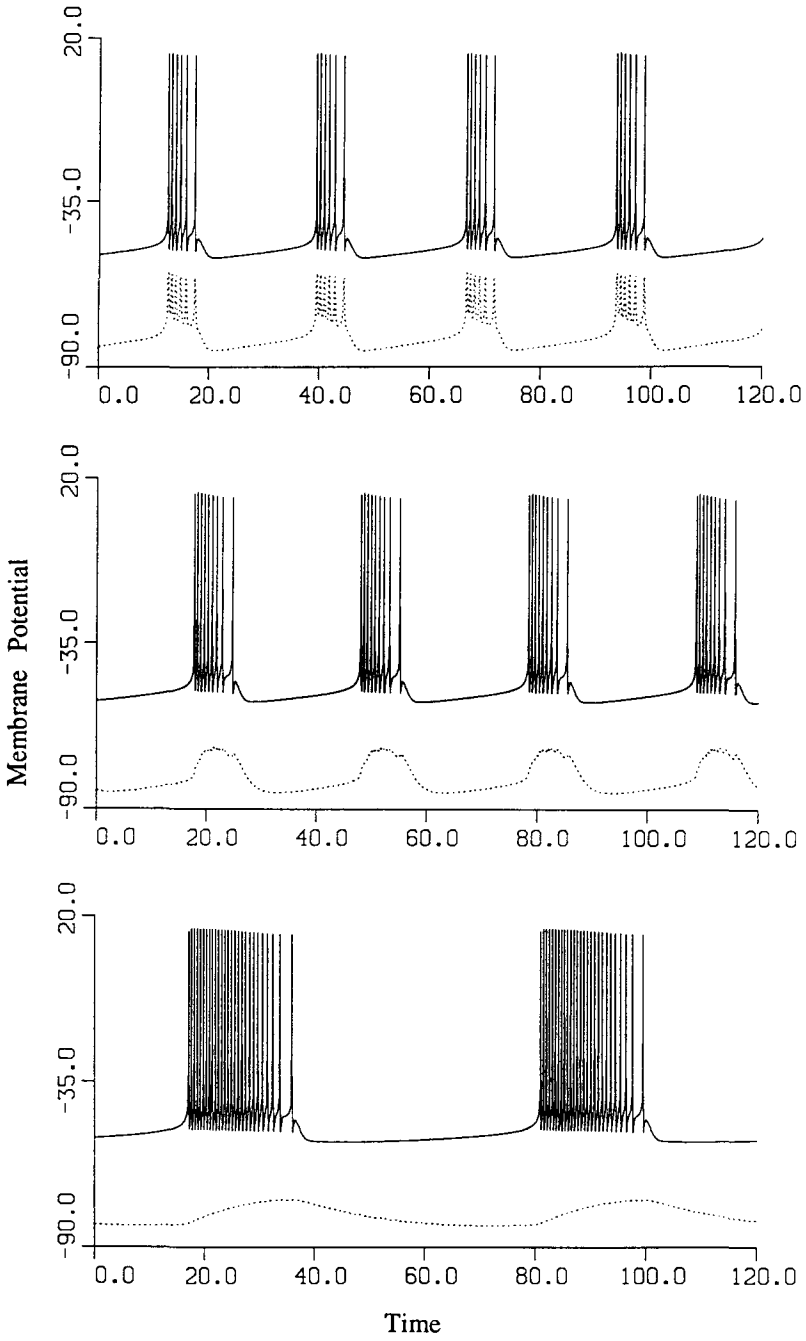

Fig. 10. The time series of electrical activity (solid lines) and the oscillation in the Ca^{2+} concentration, $[Ca^{2+}]_i$ (dashed curves) of a neuron based on the hypothesis of a Ca^{2+} -blockable Ca^{2+} channel. Note that the pattern of $[Ca^{2+}]_i$ oscillations is very different for different ρ values. From the top trace to the bottom, $\rho = 20$, 1, and 0.1. The value of g_{slow} used for this computation is 18.

periodicity), on the other hand, is controlled by the pump activity k_{Ca} and the dissociation constant K_{Ca} (whose effect comes in through σ) such that the larger the value of k_{Ca} or K_{Ca} is the longer the plateau fraction becomes.

It is important to note that all the existing neuronal models [e.g., Canavier *et al.*, 1991; Epstein & Marder, 1990; Plant, 1981; Rinzel & Lee, 1987; also some of the models in Appendix III] excluding ours [Chay, 1983, 1990; Chay & Lee, 1990; Chay & Fan, 1993] utilize $[Ca^{2+}]_i$ as a slow dynamic variable. According to all those models except ours, the slow accumulation of $[Ca^{2+}]_i$ leads to the termination of the active spiking phase, and thus V is

out of phase with $[Ca^{2+}]_i$ (as in the third trace in Fig. 10). Measurements with Ca^{2+}-sensitive dyes in various cells indicate that $[Ca^{2+}]_i$ changes rather quickly with varying membrane potential. Thus, the assumption that $[Ca^{2+}]_i$ changes slowly may not be valid any more. In our two-state (blocked and unblocked) model in which the rate of blocking is Ca^{2+}-sensitive [as in Eq. (2.5), Appendix II, Models C & D in Appendix III] the slow accumulation of $[Ca^{2+}]_i$ is not a necessary requirement for the bursting. As discussed above, the apparent rate of the blocking/unblocking event (or phosphorylation/dephosphorylation) determines the burst periodicity.

2.10. *Bifurcation diagram for the second model*

As shown in Fig. 11, AUTO predicts several interesting periodic branches when $\rho = 20$. There are four Hopf bifurcation points from which four periodic branches emerge: One unstable branch emerges from HB = 19.551 and terminates in a homoclinic orbit at $g_{slow} = 25.9252$ with an infinite period. Another one emerges from HB = 20.9737 and terminates when it meets the periodic branch from the first branch at $g_{slow} = 21.0863$. A periodic branch emerges from the right-most HB ($g_{slow} = 114.0568$) and extends to the periodic limit point at $g_{slow} = 114.852$. From there, its amplitude grows, and as its amplitude grows this periodic branch becomes stable. Then, this stable periodic state stretches to the left and terminates in a homoclinic orbit at $g_{slow} = 19.500$ with an infinite period. In this branch, the spiking mode predominates. The fourth periodic branch emerges from the left-most HB ($g_{slow} = 17.3965$); its amplitude grows suddenly at the periodic limit point of $g_{slow} = 17.36864$ (see the inset). From there, it becomes very difficult for AUTO to trace this branch. Below $g_{slow} = 17.36864$ exists the repolarized phase, and above $g_{slow} = 114.852$ exists the depolarized phase. Between the left periodic limit point (LPL = 17.3686) to the left Hopf bifurcation (LHB = 17.3965) exists three states — unstable and stable periodic states and the stable steady state (see the inset). Thus, AUTO predicts that there is a complex oscillatory region between the left most periodic limit point ($g_{slow} = 17.3686$) and the periodic limit point of the first branch ($g_{slow} = 25.9252$).

The complex structure which AUTO predicts can be seen more clearly through a bifurcation

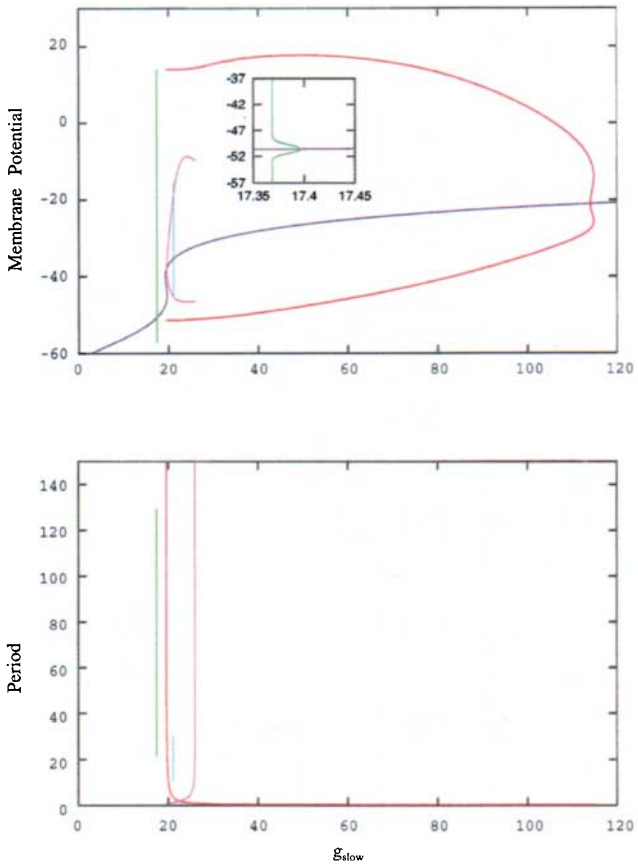

Fig. 11. Bifurcation diagram constructed using AUTO for the model based on the Ca^{2+}-blockable Ca^{2+} channel. The upper frame shows the maximum and minimum of the membrane potential V as a function of g_{slow} (the maximal conductance of the slow inward current), and the lower frame shows the periods of oscillations in the periodic branches shown in the upper frame. The inset shows the neighborhood of the left-most Hopf bifurcation, where the stable period, unstable period, and repolarized resting state coexist. We used those parameters given in the text with $\rho = 20$.

diagram constructed by solving the six differential equations in the model. Figure 12 is such a diagram obtained from the dynamic solution, where the ordinate displays f (the inactivation variable or the availability of Ca^{2+} channels) and the abscissa displays g_{slow} (the maximal conductance of the slow inward current). The two insets are enlarged portions of the left- and right-most regions of the diagram. The points in Fig. 12 (f values) for a given g_{slow} were obtained as follows: We first throw away a few hundred cycles to ensure that the system reaches the limit cycle. We then record all the f values whenever the upstroke of V passes the line $V = -30$ mV. Consistent with the AUTO prediction, this diagram reveals that the bursting bifurcates to

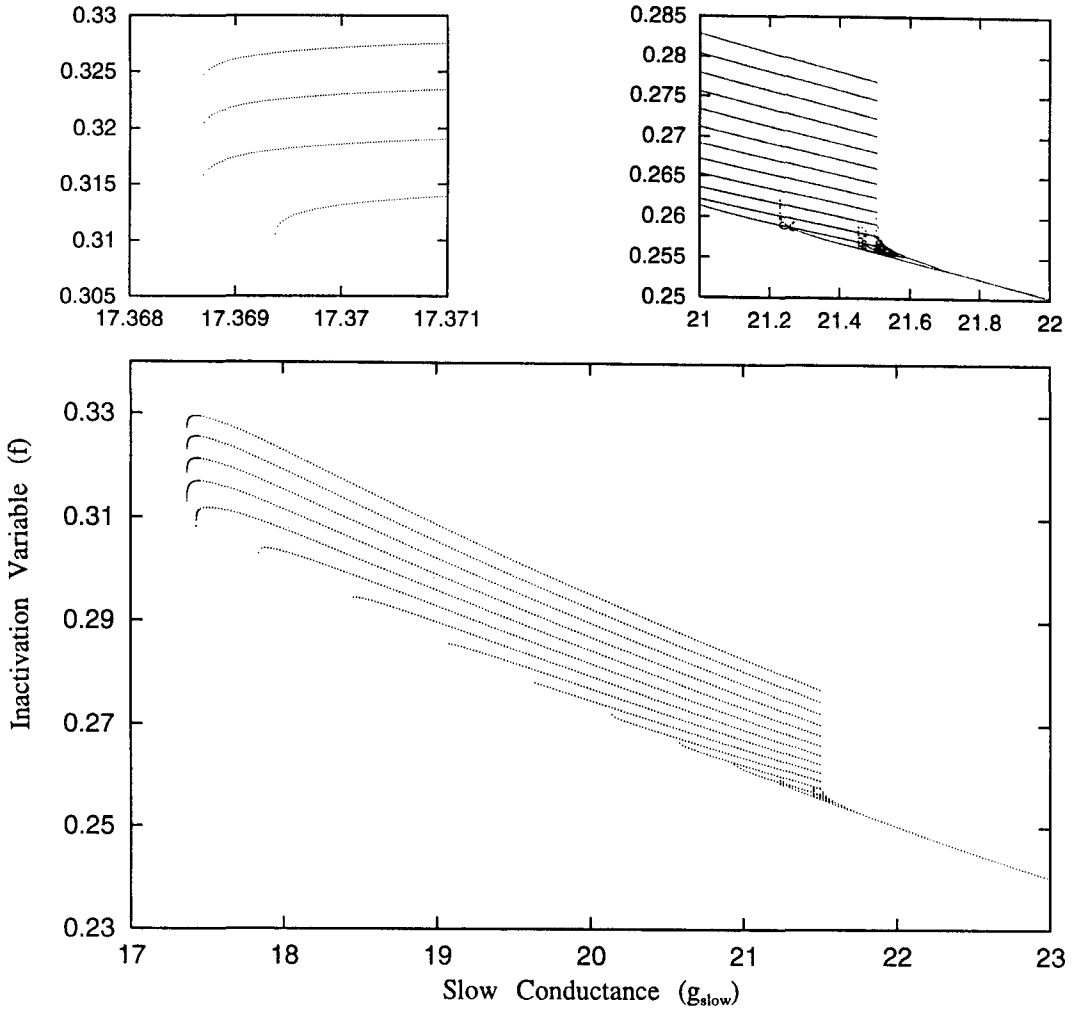

Fig. 12. Bifurcation diagram as a function of g_{slow}, which reveals the bifurcating structure of the inactivation gating variable, f, of the Ca^{2+}-blockable Ca^{2+} channel. According to the modern view of channel dynamics, f can be interpreted as the fraction of available Ca^{2+} channels at time t. The inset on the left reveals the region where the bursting regime starts, and the inset on the right reveals chaos in the crisis transition zone where the bifurcation structure suddenly shrinks.

chaos and chaos to spiking as g_{slow} increases from $g_{slow} = 17.0$ to $g_{slow} = 23$. As in Fig. 6, this model also gives rise to a spike splitting scenario. It begins with the bursting with two spikes at 17.3686 and three spikes at $g_{slow} = 17.3688$ (see the left inset). The three-spike bursting then transforms to four-spike bursting at $g_{slow} = 17.3694$. The fourth spike will eventually split into thirteen spikes as g_{slow} increases to 21.45. Beyond this point, bursting-chaos appears that transforms to spiking-chaos at the interior crisis. After this spiking-chaotic regime comes an inverse period-doubling route which leads to regular repetitive spiking at $g_{slow} = 21.7$. It is interesting to note that the bifurcating structure of the right-most chaotic regime (see the inset on the upper right) resembles closely frame (c) in Fig. 6.

As in Fig. 7, there appears a complex dynamic structure at the transition zone between the n-spike bursting and $n + 1$-spike bursting when a sufficient number of spikes is added. At which stage of the spike-splitting scenario the complex structure appears can be predicted by examining the way that a spike is born. Note that in the first four spike splitting series, a spike is added to the bifurcating trees from outside, giving a concave-up appearance. The next several branches also have a concave-up appearance, but they seem less concave upward than the first four branches. Afterwards, however, a spike is born from the existing branch (i.e., the bottom branch) giving a concave-down appearance. When a newly born bifurcating branch appears concave up, there is no complex regime. When it appears

concave down, there lies a complex oscillatory regime. In other words, *a complex transition zone arises whenever a spike is born from the existing attractors.* We will discuss this interesting phenomenon in detail in Sec. 2.12.

2.11. *The Feigenbaum scenario plus more for neurons!*

Figure 13 is a section of the right-most chaotic regime (complex-1). Here, frame (a) reveals how the fifteen branches of the nonchaotic attractors may induce bursting-chaos, and frame (b) shows the entire period doubling tree. The inset shows the boxed region in frame (a) at an enlarged scale. As shown in this figure, the complex-1 is really complex. On the right side of it, the route from order into chaos follows the Feigenbaum diagram of the period-doubling scenario. Out of repetitive spiking two branches bifurcate (period-2), out of these branches two branches bifurcate again (period-4), and then two branches bifurcate out of each of these again (period-8). We can follow the bifurcating tree up to period-16; afterwards chaos sets in. We find that the first four bifurcation points (b_1, b_2 b_3, and b_4) are 21.6921, 21.5895, 21.5692, 21.56488, respectively. Thus, the first two Feigenbaum ratios are $\delta_1 = 4.9950$ and $\delta_2 = 4.6990$ for this model. Note that δ_2 is already close enough to the Feigenbaum universal number of 4.6692016148.

On the left side of this chaos, we see a variety of beautiful structures. As shown in the inset there are several bands resulting from points not being uniformly distributed over this chaotic regime. As in one-dimensional discrete systems, the chaotic regime which follows the period-doubling sequence (i.e., the spiking-chaotic regime) is not simply a region of utter chaos. First, the four lines emerge from the period of four which collapses to only a few points (attractive periodic orbits) at $g_{\text{slow}} = 21.562$. Then from this junction arise three concentrated lines which give rise to the period of five at $g_{\text{slow}} = 21.558$. There are several other regular

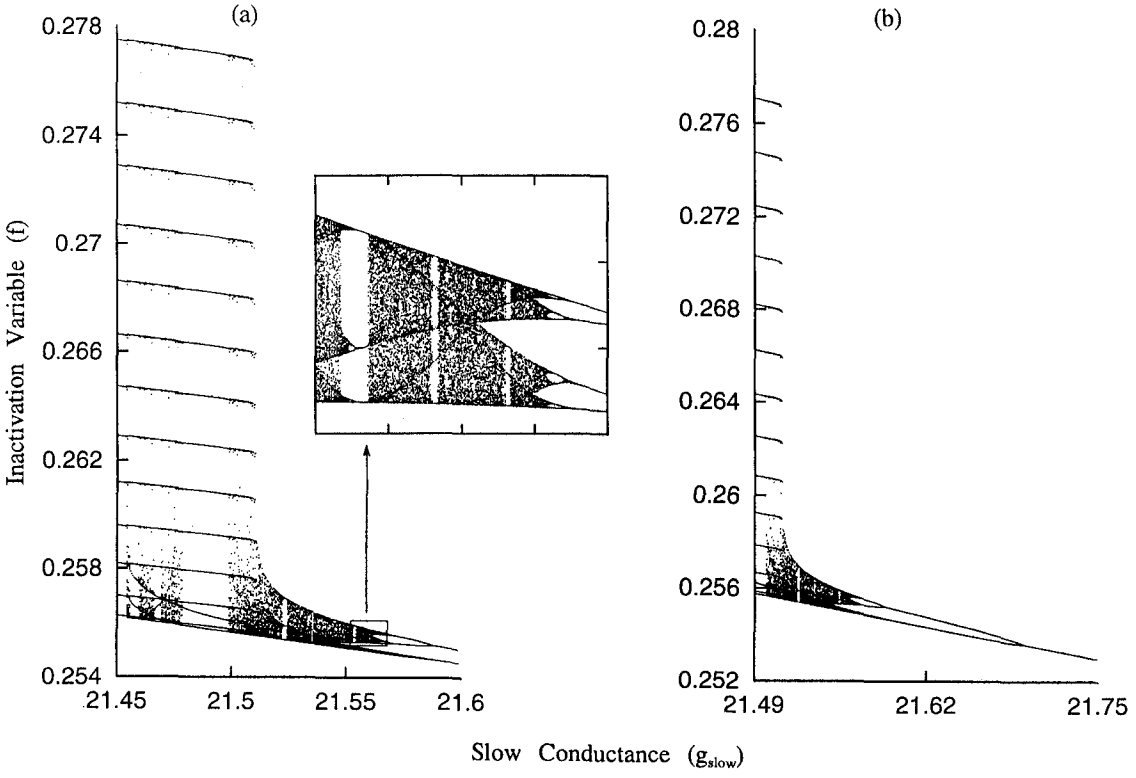

Fig. 13. The complex regimes which exist in the depolarized phase. Frame (a) shows how the thirteen-spike bursting transforms to the doublet as the system moves from the left to the right. Frame (b) shows a period doubling sequence which leads to chaotic bursting as the system moves from the right to the left. The inset is the boxed portion of frame (a) in an enlarged scale, which reveals a Feigenbaum type chaos.

periodic states embedded in this chaotic regime: The period-6 (really 12 since there are six periods from the lower branch) appears first, then the period-5 (really the period of 10), and then the period-3 (really the period of 6). At each of these bifurcation points, another periodic doubling scenario starts. Indeed, the Feigenbaum diagram is fractal, in that if a portion of the upper branch of this cascade is blown up, the resulting diagram has a self-similar structure to the original Feigenbaum tree (see the inset for evidence).

After passing this interesting chaotic regime, there arise two interesting phenomena — an interior crisis first and spike splitting series next. These scenarios do not exist in examples of one-dimensional discrete systems, but they are often observed in excitable cell models. First, a crisis transition sets in around $g_{\text{slow}} = 21.514$ where the structure suddenly expands. This expanding structure gives rise to bursting-chaos. In the bursting-chaotic regime, there appear several concentrated lines (attractive periodic orbits) — the top several attractors are more clearly defined, while the bottom ones have a diffuse appearance. This diffuse appearance become more focused as the system moves toward the left. Finally, fifteen concentrated lines clearly appear. After this scenario regular bursting appears from $g_{\text{slow}} = 21.495$. This regular bursting consists of thirteen spikes followed by two extra spikes with some pause between them.

What is the most interesting about bursting-chaos is that an odd number of attractors appears as the systems leaves the bursting chaotic regime. In other words, *only an odd number of attractors can initiate bursting-chaos* if the system moves from the left to the right. In the case of the first model bursting-chaos was set in by seven attractors (see Fig. 2.4), and in the case of the second model, fifteen attractors lead to bursting-chaos. In Chay [1985] and Canavier *et al.* [1990], the number of attractors is five for both models. In Fan & Chay [1993, 1994, 1995a,b], various odd numbers appear depending on a τ_n^* value. In some cases, the system exhibits period-doubling (in the slow wave) before entering the bursting-chaotic regime, as evidenced in Fig. 6 and in Canavier *et al.* [1990]. In other cases, however, the system enters the bursting-chaotic regime without period doubling, as seen in this figure [see frame (a)]. Bursting-chaos is semichaos in that the band of attractors farthest away from the homoclinic orbit (the bottom branch in Fig. 6 and the top branch in Fig. 12) is most "attractive." By most attractive, we mean that the location in which the chaotic attractors appear is more predictable than that in the vicinity of the homoclinic orbit.

2.12. *Complex oscillatory modes at the spike splitting junctions*

As in the first model which utilizes the Ca^{2+} activated K^+ channel mechanism, a complex dynamic structure resides at the junction where n spikes split into $n + 1$ spikes. Figure 14 reveals the structure that resides in the transition zone between eleven-spike bursting and twelve-spike bursting [frame (a)], between twelve-spike bursting and thirteen-spike bursting [frame (b)], and between thirteen-spike bursting and bursting-chaos [frame (c)]. There are several similarities between this figure and Fig. 7: First, *the dynamic structure becomes increasingly complex as more spikes are added* (i.e., as g_{slow} increases). Second, the range of the complex dynamic regime becomes wider as more spikes are added. Third, the dynamic structure contains a few chaotic states and an ordered state between them. Fourth, in the nonchaotic regime, at least two extra attractive branches are added to the basic branches. Fifth, more points (i.e., chaotic attractors) appear near the homoclinic orbit (i.e., the top band in Fig. 7 and the bottom band in Fig. 14). In other words, the attractor bands become increasingly narrower the farther they are from the homoclinic orbit, i.e., the farther the attractors are from the homoclinic orbit the more "predictable" they become.

Note in frame (a) that chaos ($C1$) exists in a very narrow range. From $C1$, the system enters the periodic state ($R1$). This regime contains eleven basic branches and two extra branches. Two extra branches are born from the bottom band of chaotic attractors. In the $R1$ regime, a burst consists of eleven spikes that are followed by two extra spikes with some pause between them. As the system moves further to the right, the two extra branches get closer to the basic branch at the bottom. This movement gives rise to chaos ($C2$). After passing $C2$, a period of twelve emerges. This periodic state consists of a burst with twelve spikes whose spike interval gets longer and longer as it approaches the termination of the active phase (i.e., normal bursting).

A complex dynamic regime that resides in frame (b) is very similar to that in frame (a), but it

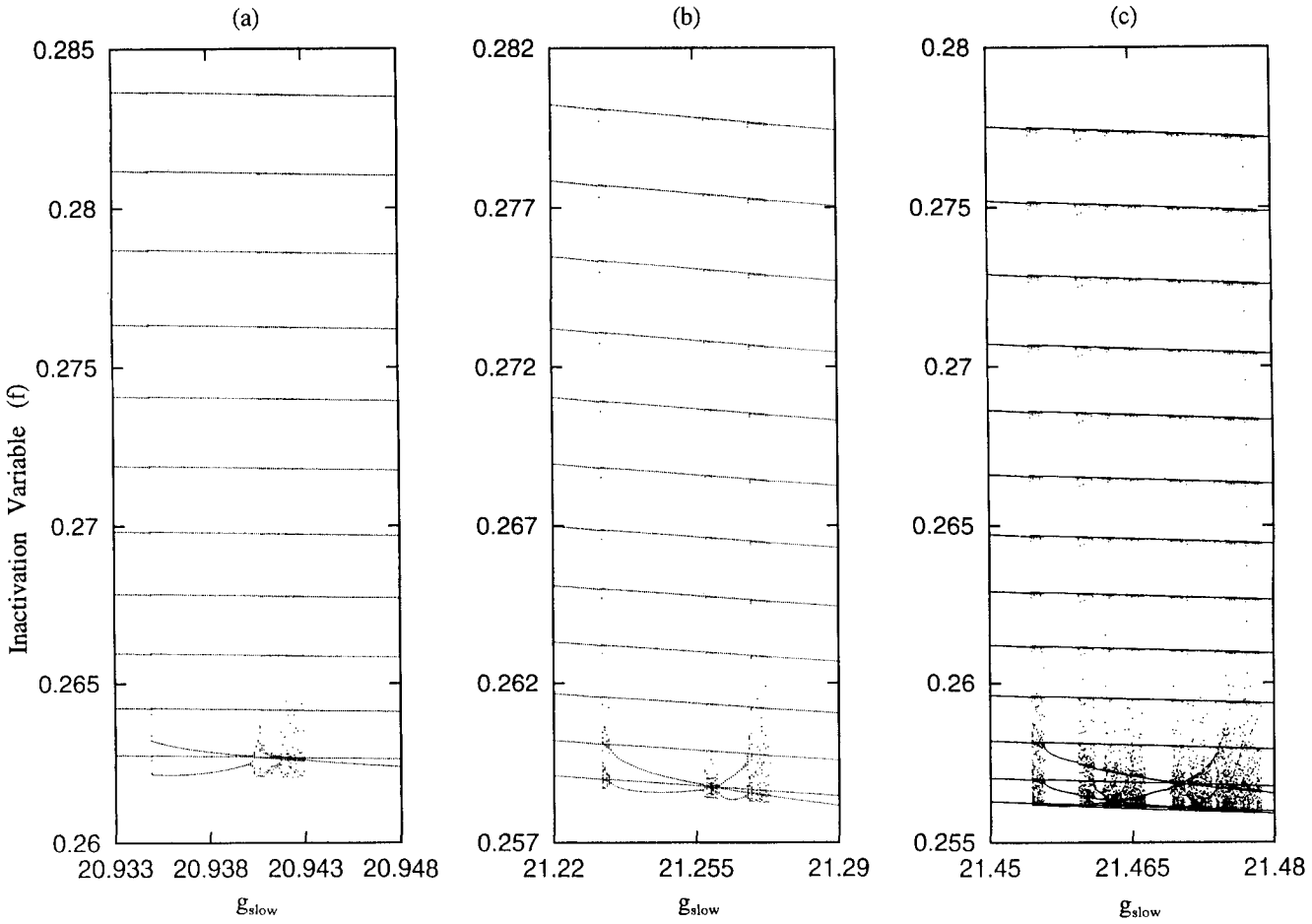

Fig. 14. Enlarged portions of the transition regimes shown in Fig. 12, where eleven spikes are split to twelve [frame (a)], twelve spikes are split to thirteen [frame (b)], and thirteen spikes are running into the bursting chaotic regime [frame (c)].

contains one additional complex regime. There are altogether three chaotic regimes ($C1$, $C2$, $C3$). Between them lie two ordered states — the left one ($R1$) with fourteen attractors and the right one ($R2$) with fifteen attractors. In $R1$, there are twelve basic branches and two extra branches that are born from the bottom two bands of chaotic attractors in $C1$. In $R2$, there are twelve basic branches and three extra branches that are born from the band of chaotic attractors at the bottom. On the boundary between $R2$ and $C3$ there is some order in the structure: at $g_{\text{slow}} = 21.265$ a period of fifteen spikes appears (thirteen basic spikes plus two extra spikes). It then transforms to sixteen spikes (thirteen basic spikes plus three extra spikes) at $g_{\text{slow}} = 21.268$. As g_{slow} increases to 21.269 an alternating order of thirteen and fifteen spikes appears. When $g_{\text{slow}} = 21.270$ there arises a repeating structure with a long period consisting of the combination of thirteen, fourteen, and fifteen spikes. Afterwards chaos sets in ($C3$).

A bifurcating structure in frame (c) is much more complex than the previous two bifurcating regimes. What differentiates this complex regime from that in frame (b) is that the third attractive branch (from the bottom) also contributes to the genesis of the complex dynamics. In frame (c), there are at least three ordered states embedded in this complex regime. The periodic state on the left consists of sixteen-spike bursting — thirteen basic spikes that are separated by three extra spikes. The periodic state in the middle consists of thirteen basic branches and five extra branches. The periodic states on the right consists of seventeen branches — thirteen basic ones and four extra ones. As the system leaves this complex regime, there appears a burst with fifteen spikes (thirteen basic spikes which are followed by two extra spikes). As g_{slow} is

increased to $g_{slow} = 21.478$, the system enters the bursting-chaotic regime.

Although the complex structures shown in Fig. 14 are essentially the same as those shown in Fig. 7, the way that a new spike is born in frame (c) (i.e., the last complex structure before entering complex-1) is quite different. In frame (d) of Fig. 7, only one spike is added to the bifurcation trees as the system leaves this complex regime. On the other hand, in frame (c) of Fig. 14 two new spikes are born from the bottom two branches as the system leaves this complex zone. Perhaps because of this difference, the way the system enters the complex-1 regime is quite different for the two models. In the first model, the system enters complex-1 via a period doubling route, whereas in the second model it enters abruptly. This difference may not be due to the two different mechanisms (i.e., the K^+ channel activation for the first model and the Ca^{2+} channel inactivation for the second model); rather they may be due to the value of another important bifurcation parameter we chose to study — τ_n^* in the first model, and g_{fast} (the fast conductance) in the second model. We refer the reader to a paper by Fan and Chay [1995b] to find out how delicately τ_n^* controls the bifurcation structure and the chaotic domain in the case of the first model.

2.13. *Discussion of Sec. 2*

In this section, we undertook a bifurcation analysis to cover the roles of the key ion channels in the plasma membrane in the genesis of complex oscillatory phenomenon. We considered two types of model: the first model is dependent on the Ca^{2+}-activated K^+ channel for a pacemaker current and the second model is dependent on the Ca^{2+}-blockable Ca^{2+} channel for a pacemaker current. With these two models, we showed how easily a spiking neuron can be converted to a bursting neuron when the conductance of the pacemaker current changes slightly. We furthermore showed that their bifurcating dynamic structures (as a function of the "pacemaker" conductance) are universal in the following senses. When the value of the pacemaker conductance (bifurcation parameter) is either small or very large, the cell is in the stable steady states (i.e., repolarized or depolarized state). When the bifurcation parameter is changed from the depolarized state toward the repolarized state, the system enters a complex dynamic regime (which we refer to as the complex-1 regime). In this complex regime, first, the Feigenbaum scenario sets in, which contains a period doubling route, tangent bifurcation, period-3, and interior crisis of a Feigenbaum type. Chaos that resides in the Feigenbaum scenario is named as spiking-chaos in neurobiology [Chay & Rinzel, 1985].

After passing the Feigenbaum scenario, there appears another type of interior crisis, where spiking-chaos transforms to bursting-chaos. Bursting-chaos contains several clear concentrated bands. Bursting-chaos is semichaos in that the band that is farthest away from the homoclinic orbit is most attractive and the band that is closest is least attractive. That is, points (i.e., chaotic attractors) are most concentrated in the band that is farthest away from the homoclinic point, and the band that is nearest to the homoclinic point has the most diffused appearance. As the system moves away from this chaotic regime toward the repolarized phase, each band narrows down to a single line (an attractor). What is interesting about these attractors is that there appears to be only an odd number of attractors. In other words, *only an odd number of attractors can trigger bursting-chaos* as the system enters into complex-1 from the spike splitting scenario.

After passing complex-1, there appears another type of scenario, a *spike-reducing series*. As the system enters the spike-reducing scenario, there exists an odd number of attractive branches at first, but the attractive branch at the extreme level (i.e., the top branch for the first model and the bottom branch for the second model) starts to disappear one by one. First, this attractive branch (say $A1$) disappears by merging with the attractor in the next level ($A2$). This gives the appearance that the $A1$ branch curves inward in order to merge with the $A2$ branch. In this case, a complex dynamic regime (say complex-2) arises as $A1$ merges to $A2$. This phenomenon repeats until the number of the attractive branches is sufficiently reduced (say until it reaches complex-n). Then, the way $A1$ disappears becomes quite interesting — instead of merging to $A2$, it runs away from $A2$. This gives the appearance that the $A1$ branch curves outwardly away from other attractive branches. In this case, the spike disappears suddenly, i.e., there appears no complex dynamic regime. Within each complex regime, there reside bursting-chaos as well as periodic bursting. Complex-1 is the most complex, and complex-n is the least complex. Also, the magnitude of the largest Lyapunov exponent λ_1 is largest in the complex-1 regime, and it is smallest in

the complex-n regime. Thus, not only does λ_1 indicate the type of irregularity (i.e., deterministic chaos versus quasiperiodicity) but it also indicates a degree of irregularity of chaos (i.e., the larger the λ_1 is the more chaotic the system becomes). The degree of the complexity owes its origin to how closely the system can approach the homoclinic orbit. The range in which complex-1 resides is the widest, and complex-n is the narrowest.

The features that arise after the Feigenbaum scenario have not yet been observed in discrete one-dimensional systems or any other physical system. Thus, it seems that this scenario is a unique feature of excitable cells. It would be interesting to explore experimentally the existence of such a scenario in bursting neuronal cells. At the present time, the resolution of the digitizers that record the neuronal voltage signal is not accurate enough to perform experiments where the bifurcation parameters can be precisely controlled. With the advent of improved recording techniques and isolated single cell preparation, it would be possible to verify this interesting scenario predicted by our neuronal models. By combining experiment with theory it will also be possible to find the means of controlling the neuronal chaos by adjusting the conductance of the key ion channels.

But what does it mean physiologically when the system bifurcates when the conductance of a pacemaker current varies? Varying the conductance of a channel either enhances or blocks the channel. Most epileptogenic and convulsant agents are known to be blockers of the key ion channels in the plasma membrane. Our demonstration that the blocking of the pacemaker channel can bring cells back to regularity from erratic electrical activity suggests that chaos theory may be applicable in controlling neuronal disorders. In fact, there is experimental evidence [Chalazonitis, 1978] demonstrating that the application of epileptogenic agents such as PTZ to the Helix neuronal cell leads to the appearance of abnormal bursting activity. Elimination of the drug by washing converts the cell back to repetitive rhythmic activity.

We believe that the elucidation of abnormal electrogenesis in terms of ionic mechanisms will lead to a greater understanding of the intrinsic nonlinear dynamic properties of neurons. Our findings may explain why the drugs that are used to treat neurodisorders are usually ion channel blockers. An implication of our finding is that theory of nonlinear dynamics may be used to understand and improve the treatment of epilepsy.

3. Bursting, Phase-Locking, and Fractals in the Intracellular Ca^{2+} Oscillations in NonExcitable Cells

Intracellular Ca^{2+} ions are essential for the initiation of cellular events such as the fertilization of eggs, the contraction of muscle, and the secretion of hormones and peptides. In excitable cells, an increase in intracellular Ca^{2+} ions is brought about by the Ca^{2+} channels in the plasma membrane when these channels open during depolarization, permitting calcium from the external medium to enter the cell (see Sec. 2). In nonexcitable cells (which are electrically nonresponsive), however, calcium is supplied mainly by the Ca^{2+} stores in the cytosol. These stores release Ca^{2+} when a certain type of agonist binds to the receptor embedded in the plasma membrane. There are two types of Ca^{2+} stores in the cytosol; a store that releases luminal calcium when cellular inositol (1,4,5) triphosphate becomes high (known as the IP_3-sensitive store) and another type of store that releases Ca^{2+} when $[Ca^{2+}]_i$ becomes high (known as the IP_3-insensitive store). See Fig. 15. The two Ca^{2+} stores are refilled by the Ca^{2+}-ATPase pump which pumps intracellular Ca^{2+} back to the stores. These two types of stores are also abundant in excitable cells, and thus excitable cells may make use of intracellular as well as extracellular sources of calcium to initiate and maintain cellular events [Chay, 1993a].

As is the case for most cellular events, the release of Ca^{2+} from the Ca^{2+} stores occurs in an oscillatory manner. For a given agonist, the concentration of the agonist has little influence on the amplitude, but it has a great influence on the frequency of the oscillation, i.e., this oscillation is a frequency-encoded oscillation. So, the question is, why and how does $[Ca^{2+}]_i$ oscillate when the cell senses the agonist? Using a "one-pool" model introduced in Sec. 3.1, we will show in Secs. 3.2 and 3.3 how the bifurcation structure changes when the agonist concentration varies. The case treated in these two sections is in the steady presence of the agonist. Under *in vivo* conditions, however, the brain releases neurotransmitters and hormones in a pulsatile fashion. Thus, how $[Ca^{2+}]_i$ responds to a pulsatile application of agonist is of more physiological significance. In Secs. 3.4 and 3.5 we will show that the response of $[Ca^{2+}]_i$ to brief repetitive

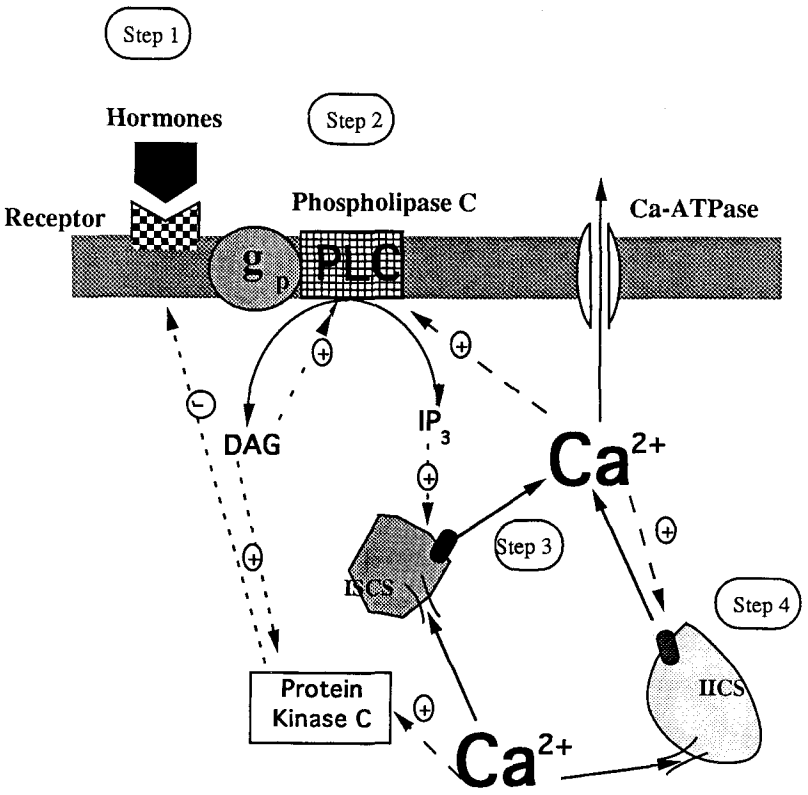

Fig. 15. Types of intracellular calcium stores and the role of G-proteins. This diagram depicts how the intracellular calcium concentration rises when certain hormones or neurotransmitters bind to their receptors in the plasma membrane of nonexcitable cells. Here, g_p stands for the GTP-bound g-protein, IP_3 for inositol $(1,4,5)$ triphosphate, DAG for diacylglycerol, ISCS for the IP_3-sensitive Ca^{2+} store, and IICS for the IP_3-insensitive Ca^{2+} store.

application of the agonist follows the universality rule that exists in theory of nonlinear dynamics. In the remaining sections, we will treat a "two-pool" model and show that the participation of the second Ca^{2+} store gives rise to a complex bifurcating structure similar to that of electrical bursting in neurons.

3.1. *A model which includes only one type of calcium store (i.e., an IP_3-sensitive store)*

The first model of a nonexcitable cell that we will consider is based on Example 1 of Cuthbertson and Chay [1991] with a few modifications as presented in Chay [1993a]. This model includes the following sequence of events (see Fig. 15). When certain types of hormones and neurotransmitters are bound to their receptors in the plasma membrane, the GDP-bound g-protein (g-GDP) is converted to G_α-GTP (GTP-bound g-protein). See Step 1. The activated form of the g-protein, G_α-GTP, together with Ca^{2+} ions can activate phospholipase C (PLC). Activated phospholipase C can produce two important cellular messengers from phosphatidyl inositol (4, 5) biphosphate (PIP2). These messengers are inositol $(1,4,5)$ triphosphate ($InsP_3$) and diacylglycerol (DAG). See Step 2 in Fig. 15. A positive-feedback by DAG makes the production of DAG and IP_3 very cooperative (although this step is not a requirement). The IP_3 thus produced can release Ca^{2+} ions from the IP_3-sensitive calcium store (ISCS) by activating the Ca^{2+} channels in this store. See Step 3 in the same figure. At the same time, protein kinase C (PKC) activity is enhanced because of combined elevations of DAG and cytosolic Ca^{2+}. Activated PKC inhibits G_α-GTP via phosphorylation. The phosphorylation of G_α-GTP inactivates PLC, which in turn leads to lowering of the $InsP_3$ level. The oscillatory cycle thus is initiated.

The first step shown in Fig. 15 can be described by the equation below:

$$\frac{d[G_\alpha - GTP]}{dt} = r_g - h_g R_{PKC}[G_\alpha - GTP] \quad (3.1)$$

where $[G_\alpha\text{-GTP}]$ is the concentration of a receptor bounded GTP-bound g-protein, and R_{PKC} is the activity of PKC which is a function of both [DAG] and $[Ca^{2+}]_i$:

$$R_{PKC} = \frac{[DAG]}{K_p + [DAG]} \frac{[Ca^{2+}]_i}{K_c + [Ca^{2+}]_i} .$$

Here, K_p and K_c are the dissociation constants of DAG and Ca^{2+} from their respective receptor sites in PKC. In Eq. (3.1), r_g is an important parameter (i.e., a bifurcation parameter) which is "proportional" to the agonist concentration.

The second step shown in Fig. 15 can be described by

$$\frac{d[DAG]}{dt} = k'_d R_{PLC} - h_d[DAG] + \ell_d ,$$
$$([DAG] = [IP_3]) , \qquad (3.2)$$

where R_{PLC} is the activity of PLC which is a function of $[Ca^{2+}]_i$,

$$R_{PLC} = \frac{[Ca^{2+}]_i^4}{K'^4_{cg} + [Ca^{2+}]_i^4} ,$$

and K'_{cg} is the dissociation constant of $[Ca^{2+}]_i$ which depends on $[G_\alpha\text{-GTP}]$ in the following manner:

$$K'_{cg} = K_{cg}\left[1 + \frac{K_g}{[G_\alpha - GTP]}\right] .$$

In Eq. (3.2), k'_d has a positive feedback from DAG such that

$$k'_d = k_d \frac{[DAG]^2}{K_d^2 + [DAG]^2} ,$$

where k_d and K_d are the rate constant and the dissociation constant, respectively.

Step 3 of Fig. 15 can be described by

$$\frac{d[Ca^{2+}]_i}{dt} = k_{ISCS} R_{IP3} - h_C[Ca^{2+}]_i + \ell_c , \qquad (3.3)$$

where R_{IP3} is the activity of the IP_3-sensitive Ca^{2+} channel in the ISCS and is enhanced by $[IP_3]$ as shown:

$$R_{IP3} = \frac{[IP_3]^3}{K_s^3 + [IP_3]^3} .$$

In Eq. (3.3), h_c measures the ATPase pump activity, and ℓ_c measures the resting Ca^{2+} level.

To reiterate, this model (which does not include the IP_3-insensitive second store) can be described by three variables, $[G_\alpha\text{-GTP}]$ [Eq. (3.1)], [DAG] [Eq. (3.2)], and $[Ca^{2+}]_i$ [Eq. (3.3)], given above. The basic parametric values in the model are: $r_g = 2.0$ nM·s^{-1}, $h_g = 10$ s^{-1}, $k_d = 4.0 \times 10^5$ nM·s^{-1}, $h_d = 8$ s^{-1}, $\ell_d = 0.6$ nM·s^{-1}, $k_{ISCS} = 500$ nM s^{-1}, $h_c = 0.5$ s^{-1}, $\ell_c = 100$ nM·s^{-1}, $K_p = 40$ nM, $K_c = 500$ nM, $K_d = 5$ nM, $K_{cg} = 500$ nM, $K_g = 50$ nM, and $K_s = 5$ nM.

3.2. *Dynamic solution in the presence of only one store*

Figure 16 shows the time series of $[Ca^{2+}]_i$ (solid) and $[G_\alpha\text{-GTP}]$ (dashes) at four different values of r_g. In this model, the agonist concentration is modeled by r_g [see Eq. (3.1)], such that as the agonist concentration increases r_g also increases. The top and bottom traces show, respectively, the oscillations of $[Ca^{2+}]_i$ and $[G_\alpha\text{-GTP}]$ at very low and very high agonist concentrations. The middle two traces are those occurring in the presence of moderate agonist concentrations. Note that the period of oscillations ranges from several minutes to several seconds as r_g increases. Note also that $[G_\alpha\text{-GTP}]$ builds up slowly while $[Ca^{2+}]_i$ is at its resting level of 200 nM. When $[G_\alpha\text{-GTP}]$ reaches a critical level (~60 nM), there is a sudden release of luminal Ca^{2+} from the ISCS. This release causes a sudden increase in $[Ca^{2+}]_i$, allowing it reach above 600 nM. The increase in $[Ca^{2+}]_i$, in turn, activates protein kinase C (PKC) whose activity is determined by $[Ca^{2+}]_i$ and [DAG]. Activation of PKC causes a drop of $[G_\alpha\text{-GTP}]$ due to phosphorylation of g-proteins. As shown in this figure, the decrease of $[G_\alpha\text{-GTP}]$ is rather sudden, while $[Ca^{2+}]_i$ decreases in an exponential fashion. The decrease of $[Ca^{2+}]_i$ is due to refilling of ISCS by the action of the ATPase pump. In this model, the Ca^{2+} oscillation is driven by the pulsatile appearance of IP_3 (not shown), as in the model of Meyer & Stryer [1988]. The period of the $[Ca^{2+}]_i$ oscillation is determined by the rate of the build-up of $[G_\alpha\text{-GTP}]$, i.e., the lower the r_g value, the longer it takes to reach the maximum level of $[G_\alpha\text{-GTP}]$.

Note that the concentration of the agonist has little effect on the shape or the width of the oscillations. Also, it has little influence on the amplitude of both $[Ca^{2+}]_i$ and $[G_\alpha\text{-GTP}]$ oscillations. The frequency of the oscillations, however, depends on the agonist concentration, i.e., an increase in the agonist concentration increases the frequency. These simulation results are consistent with experiments observed in hepatocytes in the presence of phenylephrine [Wood *et al.*, 1986].

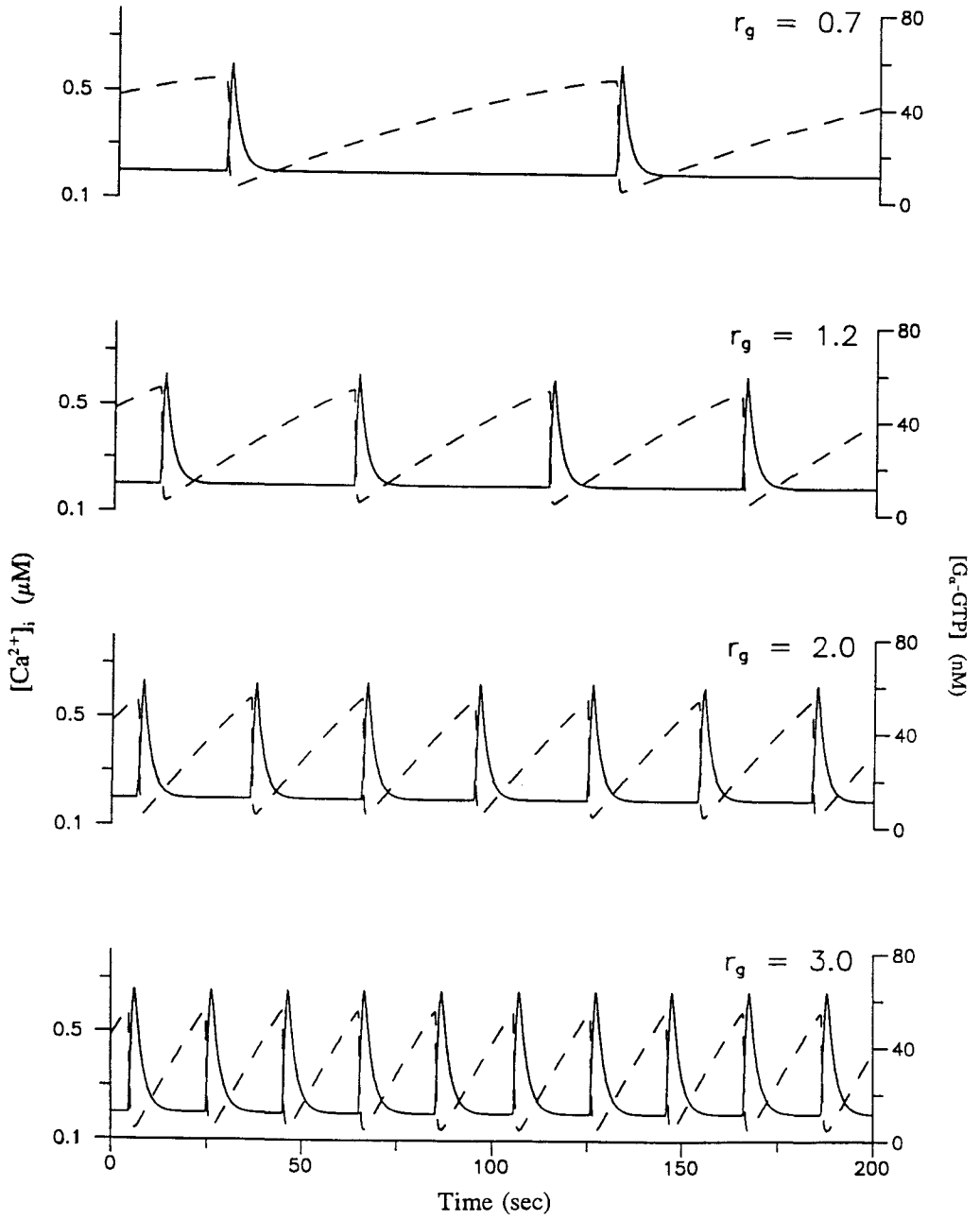

Fig. 16. Dynamic plots at four different values of r_g, the parameter that measures the strength of the agonist concentration. Here, the solid curves show the $[Ca^{2+}]_i$ oscillations, and the dashed curves show the oscillations of the slow dynamic variable $[G_\alpha$-GTP]. The top and bottom traces are picked near the left and right Hopf bifurcation points, respectively. The middle two traces are picked from intermediate agonist concentrations. The r_g values used for the computation are listed in the figure.

3.3. *AUTO analysis on the one type store*

The dynamic structure that arises from the model that is based on one type of calcium store can be seen more clearly by constructing a bifurcation diagram using r_g as a bifurcation parameter. The result of AUTO analysis is shown in Fig. 17. Here, the top frame shows the amplitude of $[Ca^{2+}]_i$ oscillation, while the bottom frame shows the corresponding period of the oscillation. The steady state branch is shown by the purple line, and the oscillatory branch is shown by the red line. AUTO predicts two Hopf bifurcation points, LHB at r_g = 0.5463 and RHB at r_g = 3.007. The periodic limit point (PLP) is located on the right side at r_g = 3.196. There are four distinct regions in this diagram: (i) the "repolarized" state below LHB

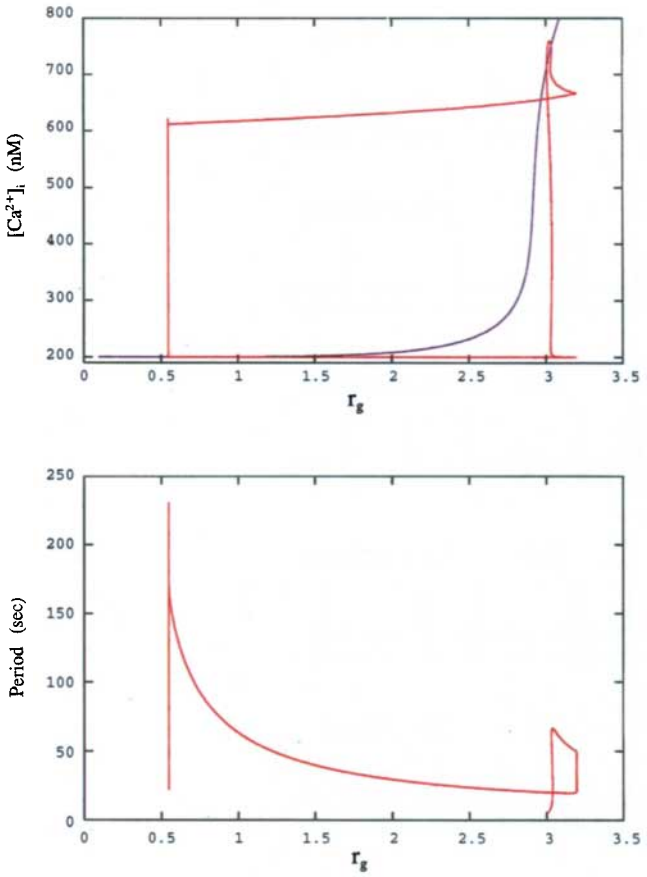

Fig. 17. AUTO result showing the effect of the concentration of an agonist on Ca^{2+}-spikes for the one-pool nonexcitable cell model. The upper frame shows the amplitude of $[Ca^{2+}]_i$ as a function of r_g, and the lower frame shows the corresponding period of oscillation. Here, the purple line is the steady state branch, the red line is the oscillatory branch.

where the cell rests at $[Ca^{2+}]_i$ of 200 nM, (ii) the oscillatory state between LHB and RHB where $[Ca^{2+}]_i$ spikes between 200 nM and 620 nM, (iii) the coexistence of two stable states, the oscillatory state and quiescent state, between RHB and PLP, and (iv) a quiescent "depolarized" state above PLP with a high $[Ca^{2+}]_i$ of above 715 nM. Note that in the oscillatory regime, r_g has little influence on the amplitude, minimum level and maximum level of the $[Ca^{2+}]_i$ oscillations. Although the amplitude is not affected by r_g, the period increases sharply as r_g is decreased from RHB to the LHB. This is consistent with the dynamic result shown in Fig. 16 where the period of oscillation in the top trace (which is near the LHB) is very long compared to that of the bottom trace (which is near the RHB). Thus, this bifurcation diagram clearly reveals that the $[Ca^{2+}]_i$ oscillation is a frequency coded one.

3.4. *Phase-locking of $[Ca^{2+}]_i$ in response to periodic stimulation of agonist*

Figure 18 shows a phase locking pattern of $[Ca^{2+}]_i$ (the upper trace) in response to repetitive agonist stimuli (the lower traces). Here, SS is a stimulus interval (i.e., the interval from the beginning of a stimulus pulse to the beginning of the next stimulus pulse). The N:M rhythm listed in this figure is defined in such a way that M stands for the number of $[Ca^{2+}]_i$ responses during N stimulus pulses; thus N is always equal to or greater than M. The square shaped stimuli shown in the lower traces (in each frame) have a base of $r_g = 0.4$ nM/sec, a height of $r_g = 2.0$ nM/sec, and a duration of 10 seconds. The stimulus strength of $r_g = 2.0$ nM/sec is not a weak stimulus (see that $r_g = 2$ corresponds to the oscillatory range in the bifurcation diagram shown in Fig. 17). The lower base (i.e., $r_g = 0.4$ nM/sec) corresponds a nonoscillatory condition, where the cell rest in quiescence with $[Ca^{2+}]_i = 200$ nM.

Note in Fig. 18 that as the stimulus interval decreases progressively (from the top trace to the bottom), the number of blocked $[Ca^{2+}]_i$ responses increases. Note also that the 5:4 and 4:3 rhythms (the second and third traces) exhibit a progressive lengthening of SH, the response time of $[Ca^{2+}]_i$ to a stimulus S. There is a concomitant reduction in the interval from the response to the next stimulus (HS). The lengthening of SH and the shortening of HS lead to a blocked $[Ca^{2+}]_i$ response at the Nth stimulus. The amplitude decreases slightly during the consecutive responses. The Mobitz Type II block (which occurs in abnormal heart rhythms) can also be seen in the 2:1 trace, where the SH interval is sufficiently long such that the next stimulus fails to elicit a Ca^{2+} spike. A complex 5:2 reverse Wenckebach rhythm composed of alternating 3:1 and 2:1 cycles can also be seen here (bottom trace). The dropped beats seen in this figure resemble those observed in the EKG trace of heart patients and is known as Wenckebach periodicity or Mobitz Type I block [Shrier *et al.*, 1987]. It also resemble those observed in the Purkinje cell under a repetitive periodic current stimulation [Chialvo & Jalife, 1987].

The N:M phase locking patterns seen in this figure also resemble those observed experimentally in squid axons [Hayashi *et al.*, 1982; Matsumoto *et al.*, 1987] and theoretically [Holden and Muhamad, 1984; Aihara and Matsumoto, 1987]

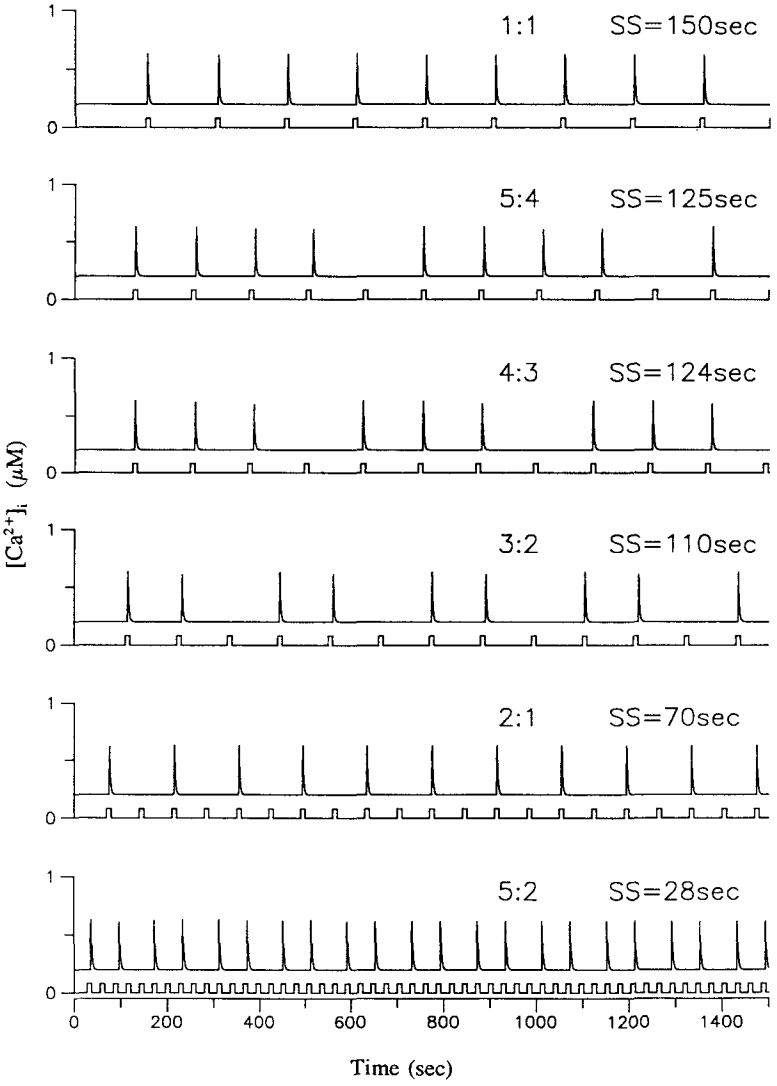

Fig. 18. Dynamic plots showing the phase-locking response of $[Ca^{2+}]_i$ for given values of the stimulus interval (SS). The stimulus intervals used for the simulation are listed in the plot. In each frame, the top trace shows $[Ca^{2+}]_i$ spikes and the lower trace shows the time course of the agonist stimulus. The strength of stimulus has a base of $r_g = 0.4$ nM/sec, a height of $r_g = 2.0$ nM/sec, and a duration of 10 seconds. Here, N:M stands for M Ca^{2+}-responses during N agonist pulse applications.

using the Hodgkin–Huxley model [Hodgkin and Huxley, 1952]. There are some differences between excitable and nonexcitable cells in their responses, however. When high-frequency periodic current pulses are applied to heart tissues, the width of action potentials changes significantly with each stimulus with little change in the height [Frame and Simson, 1988]. When high-frequency periodic agonist pulses are applied to the nonexcitable "cell", the peak of $[Ca^{2+}]_i$ spike changes with each stimulus while the shape or the width of a spike change little.

The mechanism involved in the delayed and blocked $[Ca^{2+}]_i$ rhythms observed in our simulation can be explained as follows: According to the model presented in Sec. 3.1, Ca^{2+} can only be released from the Ca^{2+} stores when $[G_\alpha$-GTP] reaches a critical level (see Fig. 16). The build-up of $[G_\alpha$-GTP] is slow, and during this slow build-up $[Ca^{2+}]_i$ remains at its resting level of 200 nM. When the agonist is pulsed prematurely, the concentration of G_α-GTP is too low to release Ca^{2+} from the store. So, a blocked response or delay arises from the model.

This mechanism of the blocked $[Ca^{2+}]_i$ response is similar to that involved in the Hodgkin–Huxley model (HH). In HH, the sodium current is the one that responds to a brief current stimulus (since it carries a depolarizing current). The inactivation

variable h of the sodium current is a slow dynamic variable. So, a dropped beat can occur when not enough sodium channels are available, which happens, for instance, when a current pulse is applied prematurely. The major difference between the excitable cell and the nonexcitable cell model is the "reaction" time, in that in the excitable cell the reaction time is of the order of milliseconds while in the nonexcitable cell it is of the order of seconds. Because of the slow reaction time, the nonexcitable cells may be ideal systems to elucidate the universal rules associated with phase-locking phenomena in biological rhythms. In fact experimental work of Schofl *et al.* [1993] indicates that such research is feasible in hepatocytes using a fluorescent dye as a probe.

3.5. *Constructing the Devil's staircase*

The manner in which blocked rhythms occur as the stimulus interval decreases can be seen more clearly in the plot shown in Fig. 19. This plot is given the name "devil's staircase" because between any two steps there is an infinity of steps, and only the devil would design such stairs. This staircase was constructed by solving three differential equations [Eqs. (3.1)–(3.3)] for a given SS value. The program used to construct this diagram contains the following features: First, SS is varied automatically by a small increment starting from $SS = 10$ and ending at $SS = 200$. For each given SS value, we record H_i, the time when the upstroke of a Ca^{2+} spike crosses $[Ca^{2+}]_i = 0.4\ \mu M$, where the subscript i stands for the ith response. We disregard the first few tens of responses so as to ensure that the data contain only the responses at the limit cycle. We then calculate the spike-to-spike intervals, $H_i - H_{i-1}$ for all i's. From the intervals thus obtained, we pick up only M distinct (and consecutive) intervals. The number N of stimuli was obtained first by computing the total time taken for the system to respond M distinct intervals and then dividing it by SS.

When the stimulus interval is long (i.e., from $SS = 127.0$ to ∞) the model gives rise to a 1:1 rhythm. In the narrow range between $SS = 126.5$ and $SS = 121.5$ exist various quasiperiodic modes whose winding number [Bak, 1977] is less than 1 but is greater than 2/3 (see the inset on the right). The time series of some of these modes are illustrated in the second and third traces of Fig. 18. Between $SS = 121.0$ and $SS = 95.0$ exists the 3:2 rhythm. The time series of this rhythm is displayed in the fourth trace of Fig. 18. In the second narrow range between $SS = 94.5$ and 92.5 exist various periodic modes whose M and N ratio is less than 0.667 but greater than 0.5 (see the top inset on the left). The 2:1 rhythm resides from $SS = 92.0$ to 35.0. As shown in the fifth trace of Fig. 18, every other response is blocked for the 2:1 rhythm. In the third narrow range between $SS = 34.5$ and 29.0 exist several modes. The M and N ratio of these modes is less than 1/2 but greater than 2/5 (see the bottom inset on the left). Then, from $SS = 28.5$ to 21.0 lies a 5:2 rhythm. The time series of this rhythm is displayed on the bottom trace of Fig. 18. From $SS = 20.5$ to 13.5 lie many periodic modes whose ratio is greater than 1/3 and less than 2/5. The basic rhythm of 3:1 appears below $SS = 13$ sec. Since the pulse duration is 10 seconds, autonomous $[Ca^{2+}]_i$ oscillations arise when SS becomes equal to or less than 10 sec.

Our staircase follows the universality rules of phase-locking nonlinear dynamic systems. An interesting feature of the staircase is that if a part of the staircase is blown up, the resulting staircase looks very much like the original curve. To illustrate this point, in Fig. 19 we have blown up three narrow regions in the staircase; (i) between the 1:1 and 3:2 region, (ii) between 3:2 and 2:1 region, and (iii) between 2:1 and 5:2 region. Between two adjacent steps there are many other types of rhythms with shorter transition zones. As shown here, the range in which the 1:1 rhythm resides is the longest and that of the 2:1 rhythm is the next longest. The range in which the 3:2 rhythm resides is shorter than that of the 1:1 or 2:1 rhythm. Our staircase also obeys the addition rule of the devil's staircase, in that between the N:M rhythm and N':M' rhythm there exist another rhythm of $(N + N')$:$(M + M')$. This addition rule was shown to hold by Keener [1981] only in the specific iterative model he studied. But it is interesting to note that this rule also holds for our nonexcitable model. Our staircase is not complete in that it starts from 0.333. As shown by Peitgen *et al.* [1992], a complete devil's staircase starts from zero and ends at one. A complete staircase has the fractal dimension of unity and the length of the boundary curve is exactly 2. Since our staircase was obtained by solving the three differential equations with a pulse duration of 10 sec, it is not possible to obtain the solution for SS equal to or less than 10 seconds.

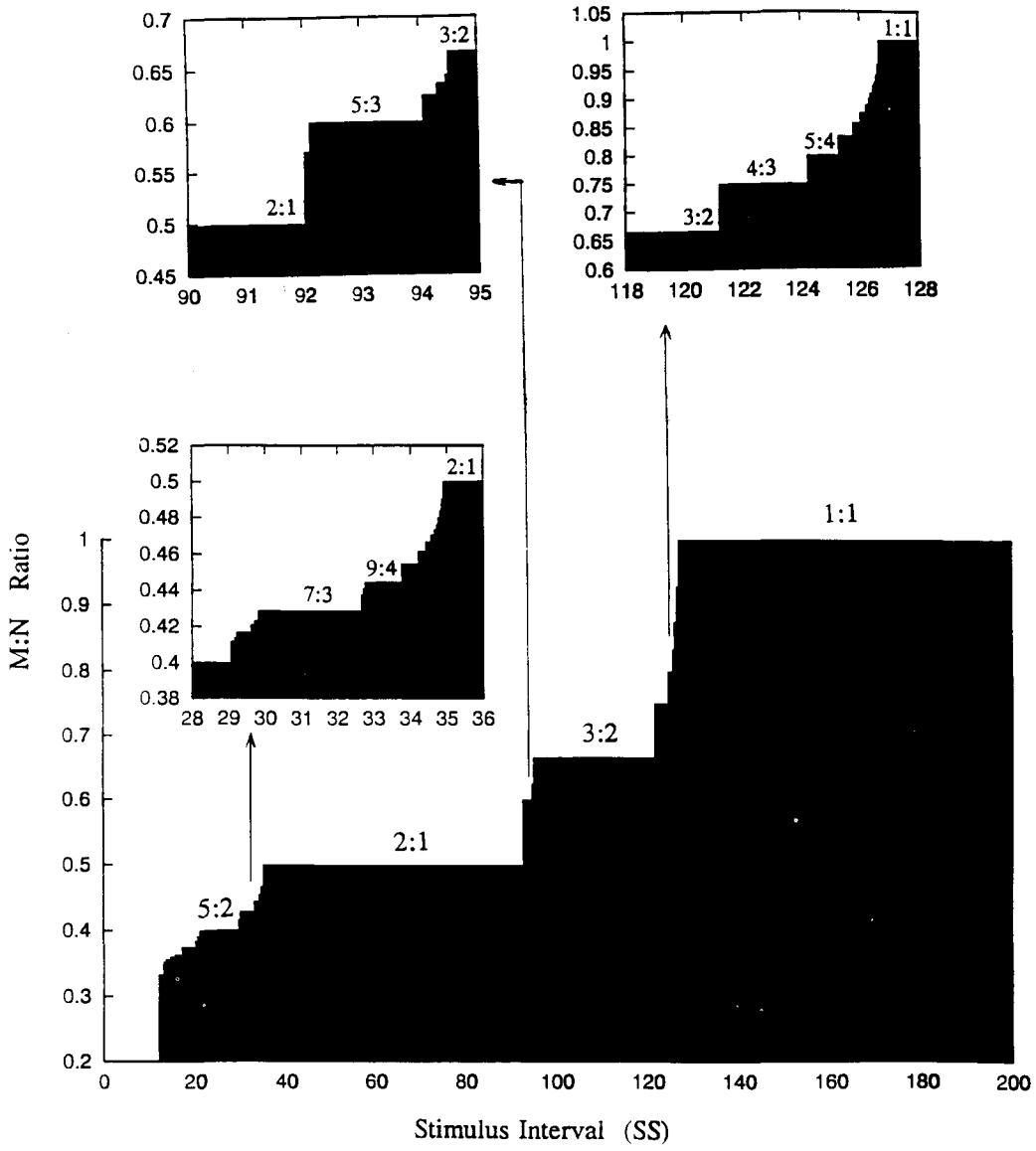

Fig. 19. Devil's staircases, M/N, as a function of the stimulus interval SS, where M is the number of Ca^{2+} spike responses and N is the number of agonist pulse stimulations. In the inset, three sections of the staircase are enlarged to demonstrate the fractal nature of the original staircase. The response was recorded whenever the upstroke of a spike crossed the $[Ca^{2+}]_i$ = 400 nM line. This diagram was constructed by solving three simultaneous differential equations in the model. The model cell was stimulated periodically at a regular interval.

3.6. *Model which includes both the IP_3-sensitive and IP_3-insensitive Ca^{2+} stores*

Why does the bursting of $[Ca^{2+}]_i$ arise in the oocyte when it "senses" a sperm (see Fig. 2) or in the hepatocyte when it is exposed to adenosine triphosphate (ATP)? As in the excitable cell model where the inclusion of the fast-gating variable n gives rise to bursting (see Sec. 2), the bursting of $[Ca^{2+}]_i$ can be induced by including a fast Ca^{2+} releasing store. The model considered here is that formulated by Chay [1993b] which includes the "fast" IP_3-insensitive calcium store (IICS) as well as the slow IP_3-sensitive store (ISCS). In this model, as in the two-variable excitable cell model of Chay & Lee [1992], it is assumed that the Ca^{2+} channel in the IICS contains a fast activating component, the "m-gate," which opens when $[Ca^{2+}]_i$ becomes high. This channel is also gated by an "h-gate," which closes slowly when $[Ca^{2+}]_i$ becomes undesirably high. The essential features of the model that includes the IICS are as follows: The events outlined in Sec. 3.1 occur first, i.e., $[Ca^{2+}]_i$ rises as a result of

the release of luminal Ca^{2+} from ISCS. Then, this rise of $[Ca^{2+}]_i$ activates the IP_3-insensitive Ca^{2+} store by the "calcium-induced-calcium release mechanism" [Fabiato, 1983; Goldbeter *et al.*, 1990]. When enough Ca^{2+} is released, the IICS will close by the Ca^{2+}-inactivation mechanism. Although for consistence with the biochemical literature we will call this calcium store IICS, what is important to our model is that release from the calcium store is calcium sensitive, that is, the release is evoked by an increase of $[Ca^{2+}]_i$.

The dynamic change of $[Ca^{2+}]_i$ now includes step 4 of Fig. 15, where the release of luminal Ca^{2+} from the IICS contributes a further increase in $[Ca^{2+}]_i$. This modifies Eq. 3.3 as

$$\frac{d[Ca^{2+}]_i}{dt} = k_{ISCS}R_{IP_3} + k_{IICS}m_\infty h - h_C[Ca^{2+}]_i + \ell_c . \qquad (3.3')$$

In the above equation, m and h are the activation and inactivation gates of the Ca^{2+} channel in IICS (which are governed by $[Ca^{2+}]_i$) and have the same significance as those described in Eq. 2.4. In this model, m_∞ is activated by $[Ca^{2+}]_i$ by the relation

$$m_\infty = \frac{[Ca^{2+}]_i^6}{K_m^6 + [Ca^{2+}]_i^6} .$$

The h-gate in Eq. 3.3' describes the closing of the channel when $[Ca^{2+}]_i$ becomes too high and has features similar to that of the Hodgkin–Huxley inactivation h-gate,

$$\frac{dh}{dt} = \alpha_h(1-h) - \beta_h h = \alpha_h\left\{(1-h) - \frac{[Ca^{2+}]_i}{K_h}h\right\}, \qquad (3.4)$$

where α_h, β_h, and K_h carry their usual meanings.

In addition to those parametric values given in Sec. 3.1, other parametric values are: K_m = 400 nM, $\alpha_h = 0.01\ s^{-1}$, and K_h = 500 nM. In this model, the degree of the participation of the second store is modeled by k_{IICS} in units of (nM s^{-1}).

3.7. *AUTO analysis to find the effect of the second type of Ca^{2+} store*

How the participation of the IP_3-insensitive Ca^{2+} store (IICS) affects the $[Ca^{2+}]_i$ oscillation can be seen via the bifurcation diagram presented in Fig. 20. Here, the bifurcation parameter, k_{IICS}, measures the degree of the participation of the IICS such that the larger the value of k_{IICS}, the stronger the effect of the second store. The upper frame shows the bifurcating structure of $[Ca^{2+}]_i$ as a function of k_{IICS}, and the lower frame shows its corresponding period. In the upper frame, the purple line is the steady state branch, and the red line is a periodic branch. AUTO predicts two Hopf bifurcation points, LHB at -7.104449×10^4 and RHB at 739.9853. As shown here, the periodic branch which evolved from the LHB connects to the RHB after reaching the periodic limit point at k_{IICS} = 1753.79. AUTO also predicts five distinct regions: (i) a region from k_{IICS} = 0 to 225.5, where $[Ca^{2+}]_i$ oscillates with a period of about 35 sec (note that

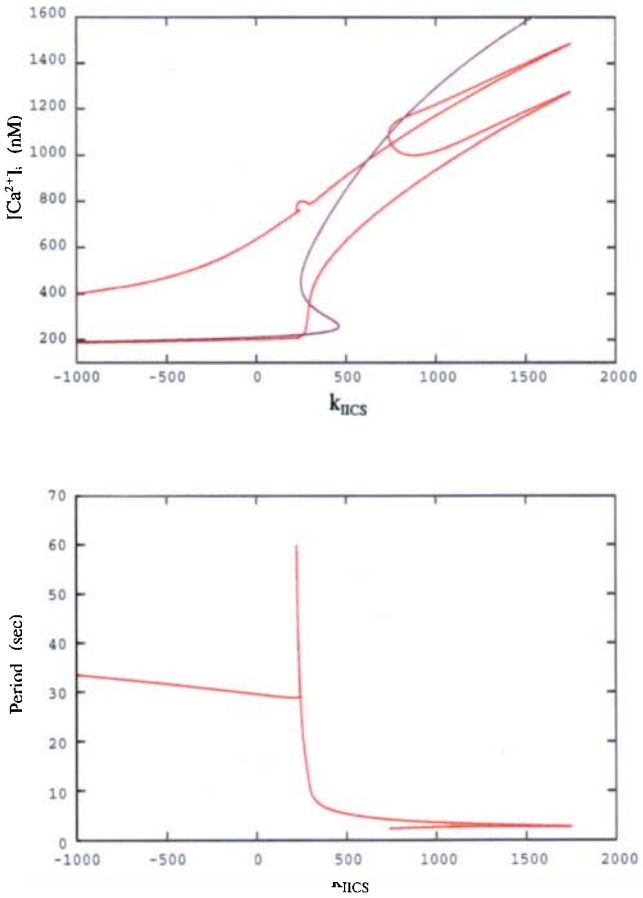

Fig. 20. Bifurcation diagram that includes an IP_3-insensitive Ca^{2+} store (IICS). The upper frame shows $[Ca^{2+}]_i$ as a function of k_{IICS} (a measure of the participation of the IICS), and the lower frame shows the period of oscillation. Here, the purple line is the steady-state branch, and the red line is the periodic branch. This bifurcation diagram was constructed using AUTO at $r_g = 2.0$.

the negative k_{IICS} is unphysiological), (ii) a "hump-back" region from $k_{\mathrm{IICS}} = 225.5$ to 291.5 where the period decreases sharply (i.e., 59.8 seconds at $k_{\mathrm{IICS}} = 225.5$ to about 10 seconds at $k_{\mathrm{IICS}} = 300$), (iii) a fast spiking region from beyond $k_{\mathrm{IICS}} = 291.5$ to RHB, (iv) a region where a fast spiking periodic state and the steady state coexist from the RHB to PLP, and (v) a quiescent "depolarized" region above PLP. This resembles the bifurcation plot of Figs. 5 and 11, which shows several interesting regions as the mode of oscillation changes from spiking to bursting as the bifurcation parameter g_p increases.

3.8. *Dynamic solutions that include the second Ca^{2+} store (i.e., IICS)*

The hump-back region [region (ii)] predicted by AUTO can be further explored by solving the four differential equations [Eqs. (3.1)–(3.4)]. The result of the solution is shown in Fig. 21. Bursts that resemble those in the excitable models (see Figs. 4 and 10) arise in the region between $k_{\mathrm{IICS}} = 225$ to 300. When k_{IICS} is small, there is a one-spike burst with low frequency (the top trace where $k_{\mathrm{IICS}} = 225$); when k_{IICS} is large the model gives

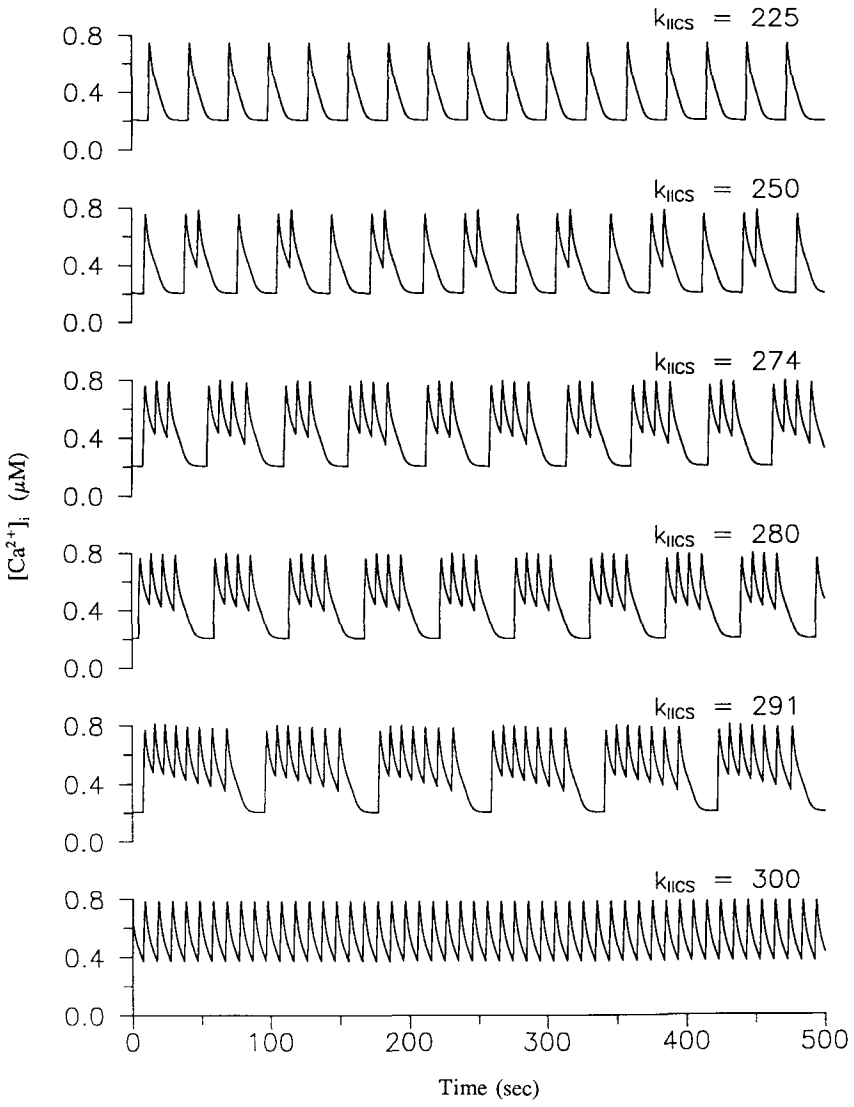

Fig. 21. Dynamic plots of $[Ca^{2+}]_i$ simulated from the model that includes two types of cellular Ca^{2+} store: $k_{\mathrm{IICS}} = 225$ (one-spike bursting), 250 (a mixture of one-and-two spike bursting), 274 (a mixture of three-and-four spike bursting), 280 (a four-spike bursting), 291 (a seven-spike bursting), and 300 (continuous spiking). The conditions are the same as Fig. 20.

rise to repetitive spiking with fast frequency (the bottom trace where $k_{\mathrm{IICS}} = 300$). Between these two modes appears a mixture of one-spike and two-spike bursts at $k_{\mathrm{IICS}} = 250$ (the second trace), a mixture of three-spike and four-spike bursts at $k_{\mathrm{IICS}} = 274$ (the third trace), a pure four-spike burst at $k_{\mathrm{IICS}} = 280$ (fourth trace), and a pure seven-spike burst at $k_{\mathrm{IICS}} = 291$ (fifth trace). We may elucidate the complex structure embedded in the bursting region systematically by constructing a bifurcation similar to that of the excitable models (see Figs. 6 and 12), and this is shown in the following section.

3.9. *Bifurcation diagram for the burst structure in nonexcitable cells*

Figure 22 shows a bifurcation diagram that reveals how the interspike intervals change as a function of k_{IICS}. This diagram was constructed by solving all four differential equations at a given k_{IICS} starting from $k_{\mathrm{IICS}} = 200$ and increasing this value incrementally until it reaches $k_{\mathrm{IICS}} = 380$. The points in this figure (which are the spike to spike intervals) were obtained by recording the time at which the upstroke of a Ca^{2+} spike crosses $[Ca^{2+}]_i = 0.4\ \mu M$ for each given k_{IICS} value. Note that the bifurcation structure of the nonexcitable cell is very similar to that of excitable cells (cf. Fig. 6). These similarities include: low frequency one-spike bursting at the "repolarized" phase (i.e., small k_{IICS} value) and high frequency spiking at the "depolarized" phase (i.e., large k_{IICS} value), a spike splitting scenario where the spikes split one by one until seven spikes are reached, and the complex oscillatory regime in the transition zone between the n- and $n+1$-spike burstings (see the inset). Thus, there seems to be universal rules associated with the bursting phenomena whether the origin of the bursting is electrical or cellular.

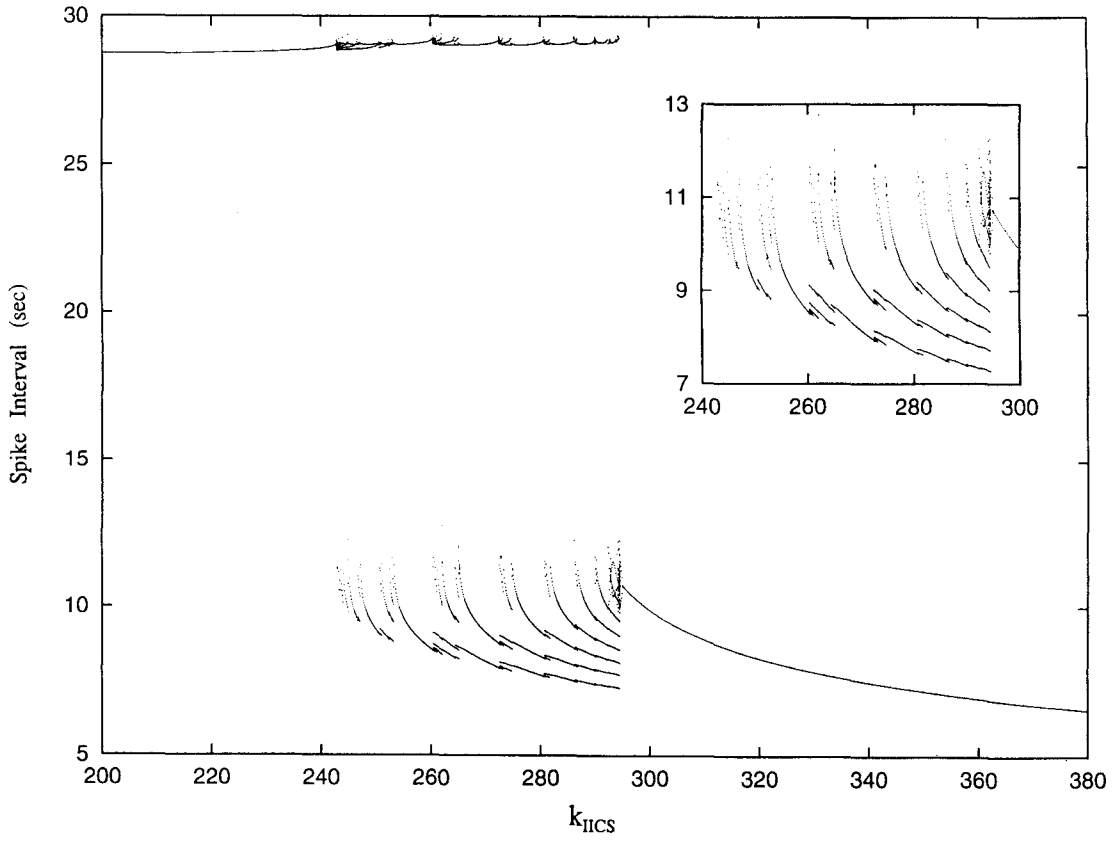

Fig. 22. Bifurcation diagram obtained by solving the four dynamic variables in this model. The ordinate shows the spike-to-spike interval (the time interval taken by two consecutive spikes as they cross the $[Ca^{2+}]_i = 400$ nM line of the upstroke). In the inset, we show the bursting regime in an expanded scale. The condition is the same as Fig. 20.

In the complex oscillatory regime where n spikes are splitted into $n + 1$ spikes, two modes of oscillations coexist — n-spike bursting and $n + 1$-spike bursting. The complex structures shown in the seven coexistence regions are not chaotic but consist of a mixture of n and $n + 1$ spikes in a regular interval. At the boundary which faces the periodic n-spike bursting (i.e., on the left boundary), the n-spiking bursting predominates over the $n+1$-bursting, while on the right boundary the reverse is true. In the middle of the boundary, the two modes of burstings appear in an alternating order (see the second and third traces of Fig. 21). For example, in the complex regime where one and two spikes coexist, at first the bursting consists mainly of one-spike bursting with occasional (but regular) appearances of a two-spike burster. However, as the system moves toward the right two-spike bursters appear more frequently. As the system is about to move out of this transition zone, the bursting consists mainly of two-spike bursters with occasional (but regular) appearances of a one-spike burster. This aspect of the complex dynamics is different from that observed in the excitable cell model where chaos is embedded in the bifurcating region where n spikes split to $n + 1$ (see Figs. 7 and 14). In this complex regime, there are more than two modes of oscillations which coexist.

Those thick bands with interspike interval of about 28 seconds are the regimes in which two modes of bursting coexist. Note that the range in which the two modes coexist shortens as the number of spikes increases. That is, the complex regime in which one- and two-spike burstings coexist is the longest, and the regime in which six- and seven-spike burstings coexist is the shortest. This reminds one of the complex dynamic structure occurring in the excitable cell models (see Figs. 7 and 14) but exactly in the opposite way. In the excitable cell model, the complex regime becomes longer and longer as the number of spikes increases.

3.10. *Discussion of Sec. 3*

We have demonstrated in this section that through an approach based on bifurcation analysis we can elucidate the rich dynamic structures that are embedded in the model of a nonexcitable cell driven by a steady application of agonist. In particular, through Figs. 17, 20, and 22, the roles of two Ca^{2+} stores in the genesis of spiking, bursting, and complex rhythms can be seen vividly when the key parameter in the model varies. The dynamic structure of these cells resembles in many ways that observed in the excitable cell models in Sec. 2, which indicates that universality may lie in the bursting mechanisms. The similarities include: (i) a spike splitting cascade when the key bifurcation parameter in the model is changed; (ii) a complex dynamic structure in the transition zone at which n-spikes split into $n + 1$-spikes; and (iii) the steady states at both ends of the bifurcation diagram. Perhaps, our future effort should be directed toward exploring both theoretically and experimentally the universality that may exist in bursting cells whether they are electrically excitable or chemically excitable. For the universality that exists in theory of nonlinear dynamics is an important subject for cell biology.

We have also demonstrated that the devil's staircases arises from nonexcitable cells when the agonist is pulsed periodically. How the $[Ca^{2+}]_i$ response entrains an agonist pulse is very important in view of the fact that the brain releases neurotransmitters and hormones periodically. The frequency of release of these agonists by the brain depends on factors such as drugs and mental state (e.g., depression or excitement). Since the release of $[Ca^{2+}]_i$ occurs in a frequency dependent manner, it is conceivable that a premature release of the neurotransmitter from the brain may cause "arrhythmias." The role of a premature agonist pulse in the Ca^{2+} release has been investigated by Chay *et al.* [1995], where we found that chaos arises at certain critical parameter values, as is the case in discrete circle maps [Jensen *et al.*, 1984]. Although phase-locking rhythms and chaos have been observed in one-dimensional maps as well as various physical systems, it is interesting to note that the same staircase also appear in the calcium release mechanism of the endoplasmic reticulum in response to agonist pulses. Because of the slow dynamics involved in the release of Ca^{2+}, calcium response entrained by neurotransmitter pulses should be a good system with which to investigate the phase-locking phenomena in biology.

The impact of a premature electrical impulse on the cardiac rhythm is obvious in that it gives rise to various cardiac arrhythmias [Chay and Lee, 1984, 1985, 1992]. Similarly, the implication of abnormal rhythms and chaos in neurobiology is clear. But, it is not clear what roles a premature agonist pulse might play in mental health, and what roles the complex bursting of $[Ca^{2+}]_i$ play in cellular physiology. This remains to be elucidated, since the study of Ca^{2+} dynamics in nonexcitable cells is

yet in its infancy. Pursuing both theoretically and experimentally this line of research (i.e., the relationship between extracellular agonist stimulation and intracellular Ca^{2+} responses), we will eventually clarify the effect of oscillations of $[Ca^{2+}]_i$ on cellular processes. We will also clarify the advantages and disadvantages of having such complex rhythms in health and disease. These studies are a contribution to what promises to be an entertaining and enlightening future in cellular Ca^{2+} dynamics.

4. Final Remark

In the past, a great deal of effort has been spent to classify and characterize the nature and types of chaos that arise in one-dimensional discrete systems [Peitgen *et al.*, 1992]. With the availability of high-speed computers and software tools such as AUTO, it is now possible to direct our efforts to more realistic physical and biological systems, where we may elucidate the universality that is known to exist in theory of nonlinear dynamics. In this review, we gave two examples in biological rhythms and have shown that such efforts are feasible and rewarding. In conclusion, we believe that many new and intriguing phenomena in nonlinear dynamics await discovery, and this is particularly so in biological rhythms. We can predict that the impact of nonlinear dynamics will then be enormous, especially in controlling and curing abnormal biological disorders such as epileptic seizures.

Acknowledgments

This work is supported by the Pennsylvania Chapter of the American Heart Association. This research was also supported in part by a grant from the Pittsburgh Supercomputing Center through the NIH Division of Research Resources cooperative agreement U41 RR0415. We thank Professor Eusebius Doedel for encouraging TRC to write this review. We also thank Drs. Stanley Smerin and Jeanne Sappington for many valuable suggestions.

References

Aihara K. & Matsumoto, G. [1987] "Forced oscillations and routes to chaos in the Hodgkin–Huxley axons and squid giant axons," in *Chaos in Biological Systems*, eds. Degn, H., Holden, A. V. & Olsen, L. F. (Plenum, New York, N.Y.).

Ammala, C., Bokvist, K., Larsson, O., Berggren, P-O. & Rorsman, P. [1993] "Demonstration of a novel apamin-insensitive calcium-activated K^+ channel in mouse pancreatic B cells," *Pflugers Arch.* **422**, 443–448.

Armstrong, D. L. [1989] "Calcium channel regulation by calcineurin, a Ca^{2+}-activated phosphatase in mammalian brain," *Trends. Neur. Sci.* **12**, 117–122.

Bak, P. [1977] "The Devil's staircase," *Physics Today* **22**, 38–45.

Berridge, M. J. & Irvine, R. F. [1989] "Inositol phosphates and cell signalling," *Nature* **341**, 197–205.

Brabant, G., Prank, K. & Schofl, C. [1992] "Pulsatile patterns in hormone secretion," *Trends Endocrinol. Metab.* **3**, 181–188.

Canavier, C. C., Clark, J. W. & Byrne, J. H. [1990] "Routes to chaos in a model of a bursting neuron," *Biophys. J.* **57**, 1245–1251.

Canavier, C. C., Clark, J. W. & Byrne, J. H. [1991] "Simulation of the bursting activity of neuron $R15$ in Aplysia: Role of ionic currents, calcium balance, and modulatory transmitters," *J. Neurobiol.* **66**, 2107–2124.

Chad, J. E. & Eckert, R. [1986] "Calcium domains associated with individual channels can account for anomalous voltage relations of Ca-dependent responses," *Biophys. J.* **45**, 993–999.

Chalazonitis, N. [1978] "Some intrinsic and synaptic properties of abnormal oscillators," in *Abnormal Neuronal Discharges*, eds. Chalazonitis, N. & Boisson, M. (Raven Press, New York), pp. 115–132.

Chay, T. R. [1983] "Eyring rate theory in excitable membranes: Application to neuronal oscillations," *J. Phys. Chem.* **87**, 2935–2940.

Chay, T. R. [1984] "Abnormal discharges and chaos in a neuronal model system," *Biological Cybernetics* **52**, 301–311.

Chay, T. R. [1985a] "Chaos in a three-variable excitable cell model," *Physica* **D16**, 233–242.

Chay, T. R. [1985b] "Glucose response to bursting-spiking pancreatic β-cells by a barrier kinetic model" *Biol. Cybern.* **52**, 339–349.

Chay, T. R. [1986] "Oscillations and chaos in the pancreatic β-cell," in *Lecture Note in Biomathematics*, ed. Othmer, H. (Springer-Verlag, New York), pp. 2–18.

Chay T. R. [1987] "The effect of inactivation of calcium channels by intracellular Ca^{2+} ions in the bursting pancreatic β-cells," *Cell Biophys.* **11**, 77–90.

Chay, T. R. [1990a] "Bursting excitable cell models by inactivation of Ca^{2+} currents," *J. Theor. Biol.* **142**, 305–315.

Chay, T. R. [1990b] "The effect of compartmentalized Ca^{2+} ions on electrical bursting activity of pancreatic β-cells," *Am. J. Physiol.* **258** (*Cell Physiol.* **27**), C55–C965.

Chay, T. R. [1990c] "Electrical bursting and intracellular Ca^{2+} oscillations in excitable cell models," *Biol. Cybernetics.* **63**, 15–23.

Chay, T. R. [1991] "Complex oscillations and chaos in a simple neuron model," *International Joint Conference on Neural Networks* (IJCNN-91-SEATTLE), II657–II662.

Chay, T. R. [1993a] "Modelling for nonlinear dynamical processes in biology." in *Patterns, Information and Chaos in Neuronal Systems*, ed. West, B. J. (World Scientific Publishing. River Edge, New Jersey), pp. 73–122.

Chay, T. R. [1993b] "The Mechanism of intracellular Ca^{2+} oscillation and electrical bursting in pancreatic β-cells," *Adv. Biophys.* **29**, 75–103.

Chay, T. R. & Cook, D. L. [1988] "Endogenous bursting patterns in excitable cells," *Math. Biosci.* **90**, 139–153.

Chay, T. R. & Fan, Y. S. [1993] "Evolution of periodic states and chaos in two types of neuronal model," in *Chaos in Biology and Medicine*, ed. Ditto, W. L., Proc. SPIE **2036**, 100–114.

Chay, T. R. & Kang, H. S. [1987] "Multiple oscillatory states and chaos in the endogenous activity of excitable cells," in *Chaos in Biological Systems*, eds. Degn, H., Holden, A. V. & Olsen, L. F. (Plenum, New York), pp. 173–181.

Chay, T. R. & Kang, H. S. [1988] "Role of single-channel stochastic noise in bursting clusters of pancreatic β-cells," *Biophys. J.* **54**, 427–435.

Chay, T. R. & Keizer, J. [1983] "Minimal model for membrane oscillations in the pancreatic β-cell," *Biophys. J.* **42**, 181–827.

Chay, T. R. & Lee, Y. S. [1984] "On impulse responses of Purkinje fibers," *Biophys. J.* **45**, 841–849.

Chay, T. R. & Lee, Y. S. [1985] "Phase resetting and bifurcation in the ventricular myocardium," *Biophys. J.* **47**, 641–651.

Chay T. R. & Lee, Y. S. [1990] "Bursting, beating, and chaos by two functionally distinct inward current inactivations in excitable cells," *Ann. N.Y. Acad. Sci.* **591**, 328–350.

Chay, T. R. & Lee, Y. S. [1992] "Studies on reentrant arrhythmias and ectopic beats in excitable tissues by bifurcation analyses," *J. Theor. Biol.* **155**, 137–171.

Chay, T. R., Lee, Y. S. & Fan, Y. S. [1994] "Phase-locking, Wenckebach-like rhythms, and devil's staircase in intracellular Ca^{2+} spikes in nonexcitable cells," *J. Theor. Biol.* **174**, 21–44.

Chay, T. R. & Rinzel, J. [1985] "Bursting, beating, and chaos in an excitable membrane model," *Biophys. J.* **47**, 357–366.

Chialvo, D. R. & Jalife, J. [1987] "Non-linear dynamics of cardiac excitation and impulse propagation," *Nature* **330**, 749–652.

Cuthbertson, K. S. R. & Chay, T. R. [1991] "Modelling receptor-controlled intracellular calcium oscillators," *Cell Calcium.* **12**, 97–108.

Cuthbertson, K. S. R. & Cobbold, P. H. [1985] "Phorbol ester and sperm activate mouse oocytes by inducing sustained oscillations in cell Ca^{2+}," *Nature* **316**, 541–542.

Doedel, E. [1981] "AUTO: A program for the automatic bifurcation analysis of autonomous systems," *Cong. Num.* **30**, 265–284.

Doedel, E. & Kernevez, J. P. [1986] "AUTO: Software for continuation and bifurcation problems in ordinary differential equation," *Applied Mathematics Report*, (California Institute of Technology).

Doedel, E., Keller, H. B. & Kernevez, J. P. [1991a] "Numerical analysis and control of bifurcation problems (I) bifurcation in finite dimensions," *Int. J. Bifurcation and Chaos.* **1**, 493–520.

Doedel E., Keller, H. B. & Kernevez, J. P. [1991b] "Numerical analysis and control of bifurcation problems (I) bifurcation in infinite dimensions," *Int. J. Bifurcation and Chaos.* **1**, 745–772.

Epstein, I. R. & Marder, E. [1990] "Multiple modes of a conditional neual oscillator," *Biol. Cybern.* **63**, 25–34.

Fabiato, A. [1983] "Calcium-induced release of calcium from the cardiac sarcoplasmic reticulum," *Am. J. Physiol.* **245**, C1–C14.

Fan, Y. S. & Chay, T. R. [1993] "Crisis transitions in excitable cell models," *Chaos, Solitons & Fractals* **3**, 603–615.

Fan Y. S. & Chay, T. R. [1994] "The generation of periodic and chaotic burstings in an excitable model," *Biol. Cybern.* **71**, 417–431.

Fan, Y. S. & Chay, T. R. [1995a] "Crisis and topological entropy," *Phys. Rev.* **51**, 1012–1019.

Fan, Y. S. & Chay, T. R. [1995b] "Bifurcations, crisis, and chaos in the Chay model of an excitable cell," *Physica D*, in press.

Fan, Y. S. & Holden, A. V. [1993] "Bifurcations, burstings, chaos and crises in the Rose-Hindmarsh model for neuronal activity," *Chaos, Solitons & Fractals* **3**, 132–143.

Feigenbaum, M. J. [1983] "Universality in nonlinear systems," *Physica* **D7**, 16–39.

Feigenbaum, M. J. [1987] "Some characterizations of strange sets," *J. Stat. Phys.* **46**, 919–924.

Frame, L. H. & Simson, M. B. [1988] "Oscillations of conduction, action potential duration and refractoriness: A mechanism for spontaneous termination of reentrant tachycardias," *Circulation* **78**, 1277–1287.

Gleick, J. [1987] *CHAOS: Making a New Science* (Viking, New York, N.Y.).

Goldbeter, A., Dupont, G. & Berridge, M. J. [1990] "Minimal model for signal-induced Ca^{2+} oscillations and for their frequency encoding through protein phosphorylation," *Proc. Natl. Acad. Sci. USA* **87**, 1461–1465.

Gorman, A. L. F., Herman, A. & Thomas, M. V. [1981] "Intracellular calcium and the control of neural pacemaker activity," *Fed. Proc.* **40**, 2233–2239.

Gorman, A. L. F., Hermann, A. & Thomas, M. V. [1982] "Ionic requirements for membrane oscillations and their dependence on the calcium concentration in a molluscan pace-maker neurone," *J. Physiol.* **327**, 185–217.

Grebogi, C. & Ott, E. [1983] "Crisis, sudden changes in chaotic attractors, and transient chaos," *Physica* **D7**, 181–200.

Hayashi, H., M. Nakao, M. & Hirakawa, K. [1982] "Chaos in the self-sustained oscillation of an excitable biological membrane under sinusoidal stimulation," *Phys. Lett.* **A88**, 265–266.

Hindmarsh, J. L. & Rose, R. M. [1982] "A model of the nerve impulse using two first-order differential equations," *Nature* **296**, 162–164.

Hindmarsh, J. L. & Rose, R. M. [1994] "A model of neuronal bursting using three coupled first order differential equations," *Proc. Roy. Soc.* **B211**, 87–102.

Hodgkin, A. & Huxley, A. F. [1952] "A quantitative description of membrane current and application to conduction and excitation in nerve," *J. Physiol. (London)* **117**, 500–544.

Holden, A. V. & Fan, Y. S. [1992a] "From simple to simple oscillatory behaviour via chaos in the Rose–Hindmarsh model for neuronal activity," *Chaos, Solitons & Fractals* **2**, 221–336.

Holden, A. V. & Fan, Y. S. [1992b] "From simple to complex oscillatory behaviour via intermittent chaos in the Rose–Hindmarsh model for neuronal activity," *Chaos, Solitons & Fractals* **2**, 349–369.

Holden, A. V. & Fan, Y. S. [1992c] "Crisis-induced chaos in the Rose–Hindmarsh model for neuronal activity," *Chaos, Solitons & Fractals* **2**, 583–595.

Holden, A. V. & Muhamad, M. A. [1984] "The identification of deterministic chaos in the activity of single neurones," *J. Electrophysiol. Tech.* **11**, 135–147.

Jensen, M. H., Bak, P. & Bohr, T. [1984] "Transition to chaos by interaction of resonances in dissicipative systems. I. Circle maps," *Phys. Rev.* **A30**, 1960–1969.

Junge, D. & Stephens, C. L. [1973] "Cyclic variation of potassium conductance in a burst-generating neurone in Aplysia," *J. Physiol.* **235**, 155–181.

Kaas-Petersen, C. [1987] "Bifurcation in the Rose–Hindmarsh and Chay models," in *Chaos in Biological Systems*, eds. Degn, H., Holden, A. V. & Olsen, L. (Plenum, New York), pp. 183–190.

Keener, J. P. [1981] "On cardiac arrhythmias: AV conduction block." *J. Math. Biol.* **12**, 215.

Kramer R. H. & Zucker R. S. [1985] "Calcium-induced inactivation of calcium current causes the inter-burst hyperpolarization of *Aplysia* bursting neurons." *J. Physiol.* **362**, 131–160.

Kriebel, M. E., Vautrin, J. & Holsapple, J. [1990] "Transmitter release: prepackaging and random mechanism or dynamic and deterministic process," *Brain Res. Rev.* **15**, 167–178.

Lee, Y. S., Chay, T. R. & Bee, T. [1983] "On the mechanism of spiking and bursting in excitable cells," *J. Biophys. Chem.* **18**, 25–34.

Matsumoto, G., Aihara, K., Hanyu, Y., Takahashi, N., Yoshizawa, S. & Nagumo, J-I. [1987] "Chaos and phase locking in normal squid axon," *Phys. Lett.* **A123**, 162–166.

Meyer, T. & Stryer, L. [1988] "Molecular model for receptor-stimulated calcium spiking," *Proc. Natl. Acad. Sci. USA* **85**, 5051–5055.

May, R. M. [1976] "Simple mathematical models with very complicated dynamics," *Nature* **261**, 459–467.

Peitgen, H-O, Jurgens, H. & Saupe, D. [1992] *Chaos and Fractals. New Frontier of Science* (Springer-Verlag. New York), pp. 220–228.

Plant, R. E. [1981] "Bifurcation and resonance in a model for bursting nerve cells," *J. Math. Biol.* **11**, 15–32.

Plant, R. E. & Kim, M. [1976] "Mathematical description of a bursting pacemaker neuron by a modification of the Hodgkin–Huxley equations," *Biophys. J.* **16**, 227–244.

Putney, J. W. & St. J. Bird, G. [1993] "The inositol phosphate-calcium signaling system in nonexcitable cells," *Endocrine Review* **14**, 610–631.

Rapp, P. E. [1993] "Chaos in the neurosciences: Cautionary tales from the frontier," *Biologist* **40**(2), 89–94.

Rinzel J. & Lee, Y. S. [1986] "On different mechanisms for membrane potential bursting," in *Lecture Note in Biomathematics* **66**, ed. Othmer, H. (Springer-Verlag, New York), pp. 19–33.

Rinzel J. & Lee, Y. S. [1987] "Dissection of a model for neuronal parabolic bursting," *J. Math. Biol.* **25**, 653–675.

Shrier, A., Dubarsky, H. D., Rosengarten, M., Guevara, M. R., Nattel, S. & Glass, L. [1987] "Prediction of complex atrioventricular conduction rhythms in humans with use of the atrioventricular nodal recovery curve," *Circulation* **76**, 1196–1205.

Schofl, C. Brabant, G. Hersch, R-D, von Zur Muhlen, A., Cobbold, P. H. & Cuthbertson, K. S. R. [1993] "Temporal patterns of α_1-receptor stimulation regulate amplitude and frequency of calcium transients," *Am. J. Physiol.* **265** (*Cell Physiol.* **34**), C1030–C1036.

Strumwasser, F. [1968] "Membrane and intracellular mechanism governing endogenous activity in neurons," in *Physiological and Biochemical Aspects of Nervous Integration*, ed. Carlson, F. D. (Prentice-Hall, Inc. New Jersey), pp. 329–341.

Wolf, A., Swift, J. B., Swinney, H. L. & Vastano, J. A. [1985] "Determining Lyapunov exponents from a time series," *Physica* **D16**, 285–317.

Woods, N. M., Cuthbertson, K. S. R. & Cobbold, P. H. [1986] "Repetitive transient rises in cytoplasmic free calcium in hormone-stimulated hepatocytes," *Nature* **319**, 600–602.

Valdeolmillos, M., Santos, R. M., Contreras, D., Soria, B. & Rosario, L. M. [1989] "Glucose-induced oscillations of intracellular Ca^{2+} concentration resembling bursting electrical activity in single mouse islets of Langerhans," *FEBS Lett.* **259**, 19–23.

Appendix I

The Rate Constants in the Ca^{2+}-sensitive K^+ Channel Model.

The expressions of the rate constants α_m, β_m, α_h, β_h, α_n, and β_n that appear in Sec. 2.1 are given in Chay [1985] and are as follows:

$$\alpha_m = \frac{0.1(25+V)}{1-e^{-0.1V-2.5}},$$

$$\beta_m = 4e^{-(V+50)/18},$$

$$\alpha_h = 0.07e^{-0.05V-2.5},$$

$$\beta_h = \frac{1}{1+e^{-0.1V-2}},$$

$$\alpha_n = \frac{0.01(20+V)}{1-e^{-0.1V-2}},$$

$$\beta_n = 0.125e^{-(V+30)/80}.$$

Appendix II

A Refined Neuronal Model Based on the Ca^{2+}-Activated K^+ Channel.

The model presented in this Appendix is the model of neurons described in Chay [1983], that gives rise to interesting patterns of bursting, spiking, and chaos, as demonstrated in Chay [1984, 1986]. A crucial difference between this model and the Plant model [1981] is the expression used for the opening probability of the pacemaker channel (i.e., the K–Ca channel), such that $[Ca^{2+}]_i$ being a slow dynamic is not required for this model. In this model, the probability of the opening of the K–Ca channel (or the fraction of available K–Ca channels) is dependent on time, Ca_i^{2+}, and voltage such that

$$\text{Closed} \underset{\lambda_p C^{-0.5}\exp(-0.5a_pV),}{\overset{\lambda_p C^{0.5}\exp(0.5a_pV)}{\rightleftharpoons}} \text{Open},$$

$$C = \left(\frac{[Ca^{2+}]_i}{K_{Ca}}\right)^{n_H},$$

where n_H is the Hill coefficient, λ_p is the rate constant independent of C and V, and K_{Ca} is the dissociation constant of Ca^{2+} ion from its receptor site located in the pore of the K^+ channel. Note that if a_p is small then the opening and closing processes of the K–Ca channel depend weakly on voltage but strongly on $[Ca^{2+}]_i$ such that its open state is favored over the closed state when $[Ca^{2+}]_i$ becomes high. Note also that this model does not assume that $[Ca^{2+}]_i$ is a slow dynamic variable. Recent measurements on $[Ca^{2+}]_i$ with fluorescent dyes indicates that $[Ca^{2+}]_i$ is a rather fast dynamic variable. This invalidates the assumption in the Plant model as well as other currently available neuronal models.

The opening probability of the K–Ca channel can be derived from the above kinetic scheme as,

$$\frac{dp}{dt} = \lambda_p(1-p)C^{0.5}\exp(0.5a_pV) - \lambda_p p C^{-0.5}\exp(-0.5a_pV),$$

where $C = [Ca^{2+}]_i/K_{Ca}$. If the kinetic process is fast (i.e., λ_p is large) then the fraction of open p can be approximated by its steady state expression:

$$p_\infty = \frac{C}{C+\exp(-a_pV)}.$$

This is the expression used by Plant where a_p is taken to be zero, but note that it has a limited applicability.

The model contains six other simultaneous differential equations:

$$-C_m\frac{dV}{dt} = m^3hJ_{Na} + dJ_{Ca} + pJ_K + n^4J_K + J_{leak} + I_{app},$$

$$\frac{dm}{dt} = \frac{m_\infty - m}{\tau_m},$$

$$\frac{dh}{dt} = \frac{h_\infty - h}{\tau_h},$$

$$\frac{dn}{dt} = \frac{n_\infty - n}{\tau_n},$$

$$\frac{dd}{dt} = \frac{d_\infty - d}{\tau_d},$$

$$\frac{d[Ca^{2+}]_i}{dt} = \frac{P_{Ca}dJ_{Ca} - k_C[Ca^{2+}]_i}{\tau_C}.$$

In this model, J_j is the flux of the jth ion expressed as

$$J_j = Z_jP_j \times \left\{C_j^{(in)}\exp\left(\frac{Z_jFV}{2RT}\right) - C_j^{(out)}\exp\left(-\frac{Z_jFV}{2RT}\right)\right\},$$

where j stands for the jth ion (i.e., Na^+, Ca^{2+}, and K^+), Z_j is the charge of the jth ion, P_j is the permeability of the jth type ion through its own ion channel, $C_j^{(in)}$ and $C_j^{(out)}$ are the concentration of the jth ion in the inside and outside the membrane, respectively, and F/RT carries its usual meaning.

For the leak flux, the model uses

$$J_{leak} = \exp\left(\frac{F(V-V_{leak})}{2RT}\right) - \exp\left(-\frac{F(V-V_{leak})}{2RT}\right).$$

The steady states m_∞, h_∞, n_∞, and d_∞, and their respective relaxation time constants τ_m, τ_h, τ_n, and τ_d take the following expressions:

$$y_\infty = \frac{\alpha_y}{\alpha_y + \beta_y} \quad \text{and} \quad \tau_y = \frac{\tau_y^*}{\alpha_y + \beta_y}$$

where α_m, β_m, α_h, β_h, α_n, and β_n take the same expression as those given in Appendix I. The rate constants, α_d and β_d, in the Ca^{2+} current take the following expressions:

$$\alpha_d = \exp(-0.5a_d(V - V_d))$$

and

$$\beta_d = \exp(-0.5a_d(V - V_d))$$

The parametric values for this model are as follows: $C_m = 1$, $I_{app} = 0.65$, $P_{Na} = 4.0$, $P_{Ca} = 0.03$, $P_{k,v} = 0.5$, $P_{k,c} = 0.2$, $P_{leak} = 0.5$, $V_d = -50$, $V_{leak} = -40$, $[Na^+]_{out} = 145$, $[Ca^{2+}]_{out} = 2$, $[K^+]_{out} = 4$, $[Na^+]_{in} = 12$, and $[K^+]_{in} = 155$, $k_C = 280$, $a_d = 0.25$, $a_p = 0.04$, $n_H = 3$, $K_{Ca} = 0.001$, $\tau_m^* = 20$, $\tau_h^* = 20$, $\tau_n^* = 20$, $\tau_d^* = 5000$, $\tau_C = 10^6$, $\lambda_p = 0.0002$, and $2RT/F = 51.2$.

Appendix III

Three-Variable Models Based on Slow Inactivation of Ca^{2+} Channel.

A minimal model that generates the bursting contain three dynamic variables — a slow dynamic variable which gives rise to an underlying slow wave, a fast dynamic variable which participates in the spiking, and membrane potential which balances the charge neutralization.

As far as we are aware, the model of Chay [1985b] is the first three-variable bursting model which incorporates the calcium-inactivated calcium channel. In this model, the inactivation variable of the calcium channel is voltage-gated, but its half-maximal potential shifts to the left as $[Ca^{2+}]_i$ increases. The Ca_i-inactivation mechanism is incorporated in this model to account for the observed extracellular Ca^{2+} effect in the pancreatic β-cell. In addition to containing the calcium-inactivated calcium channel, this model also contains the K–Ca channel which is activated by $[Ca^{2+}]_i$. Thus, the bursting occurs by the combination of both the Ca^{2+} channel inactivation mechanism and K–Ca activation mechanism via slowly varying $[Ca^{2+}]_i$.

We present in this appendix four types of three-variable models which utilizes slow inactivation of Ca^{2+} channels. These models differs from each other the way that the Ca^{2+} current inactivates and the way the spike is generated.

Model A. This model appeared in Chay [1987], and its bifurcating structure was investigated by Chay and Kang [1987]. In this model, n is a fast dynamic variable which is responsible for the genesis of spiking, and $[Ca^{2+}]_i$ is a slow dynamic variable which affects V_s, the half-maximal potential of s_∞ (one of the activation variables in the Ca^{2+} channel). That is, increasing $[Ca^{2+}]_i$ shifts V_s toward, the repolarized direction. The three simultaneous differential equations in the model is as follows:

$$C_m \frac{dV}{dt} = g_{Ca} d_\infty S_\infty (V - V_{Ca}) + g_K n(V - V_K) + g_L(V - V_L),$$

$$\frac{dn}{dt} = \frac{n_\infty - n}{\tau_n},$$

$$\frac{d[Ca^{2+}]_i}{dt} = \frac{d_\infty S_\infty (V_{Ca} - V) - k_C[Ca^{2+}]_i}{\tau_C},$$

where

$$d_\infty = \frac{1}{1 + \exp\left(\frac{V_d - V}{S_d}\right)}$$

and

$$s_\infty = \frac{1}{1 + \exp\left(\frac{V_s - V}{S_s}\right)},$$

$$V_s = S_s \ln\left(\frac{[Ca^{2+}]_i}{K_s}\right)^{n_H},$$

$$n_\infty = \frac{1}{1 + \exp\left(\frac{V_p - V}{S_n}\right)}$$

and

$$\tau_n = \frac{\tau_n^*}{1 + \exp(V - V_n)/S_n}.$$

The parametric values are: $C_m = 1$, $g_{Ca} = 55$, $g_K = 280$, $g_L = 2.2$, $V_{Ca} = 100$, $V_K = -80$, $V_L = -40$,

$V_d = -22$, $S_d = 7.5$, $V_n = -9$, $S_n = 10$, $S_s = 10$, $\tau_C = 4000$, and $\tau_n^* = 0.0085$, $K_s = 1$, $k_{Ca} = 75$, $n_H = 3$. The two bifurcation parameters that give rise to the interesting bursting and chaos behaviors are V_s and τ_n^*.

Model B. This model appeared in Chay & Kang [1988] and Chay [1991]. Its bifurcating structure was investigated by Chay & Cook [1988]. Unlike Model A, this model contains two inward currents. One of the inward currents is affected by $[Ca^{2+}]_i$, in such a way that f_∞ (the fraction of available Ca^{2+} channels) decreases with increasing $[Ca^{2+}]_i$. In this model, the spikes are caused by two types of fast currents — the fast inward current (the first term below) and the fast outward current (the third term below). The three differential equations in this model are as follows:

$$-C_m\frac{dV}{dt} = g_f m_\infty(V - V_f) + g_s d_\infty f_\infty(V - V_s) + g_K n(V - V_K) + g_L(V - V_L),$$

$$\frac{dn}{dt} = \frac{n_\infty - n}{\tau_n},$$

$$\frac{d[Ca^{2+}]_i}{dt} = \frac{d_\infty f_\infty(V_s - V) - k_C[Ca^{2+}]_i}{\tau_C},$$

where

$$m_\infty = \frac{1}{1 + \exp\left(\frac{V_m - V}{S_m}\right)}$$

and

$$d_\infty = \frac{1}{1 + \exp\left(\frac{V_d - V}{S_d}\right)},$$

$$f_\infty = \frac{1}{1 + C} \quad \text{where} \quad C = \frac{[Ca^{2+}]_i}{K_f},$$

$$n_\infty = \frac{1}{1 + \exp\left(\frac{V_n - V}{S_n}\right)}$$

and

$$\tau_n = \frac{\tau_n^*}{1 + \exp(V - V_n)/S_n}.$$

The parametric values are: $C_m = 1$, $g_f = 60$, $g_s = 25$, $g_K = 110$, $g_L = 25$, $V_f = 40$, $V_s = 110$, $V_K = -80$, $V_L = -60$, $V_m = -18$, $S_m = 8$, $V_d = -40$, $S_d = 8$, $V_n = -10$, $S_n = 8$, $\tau_C = 40$, $\tau_n^* = 0.026$, $K_f = 1.0$, and $k_C = 2.0$. The two bifurcation parameters that give rise to the interesting bursting and chaos behaviors are k_C and τ_n^*.

Model C. This model was presented in Chay [1990a] and Chay & Lee [1990]. In this model f is a slow dynamic variable which depends on time and voltage. This model differs from Models A and B in that it does not have any $[Ca^{2+}]_i$ dependent component. The three differential equations in this model are as follows:

$$-C_m\frac{dV}{dt} = g_s d_\infty f(V - V_s) + g_K n(V - V_K) + g_L(V - V_L),$$

$$\frac{df}{dt} = \frac{f_\infty - f}{\tau_f},$$

$$\frac{dn}{dt} = \frac{n_\infty - n}{\tau_n},$$

where

$$d_\infty = \frac{1}{1 + \exp\left(\frac{V_d - V}{S_d}\right)},$$

$$f_\infty = \frac{1}{1 + \exp\left(\frac{V_f - V}{S_f}\right)},$$

and

$$n_\infty = \frac{1}{1 + \exp\left(\frac{V_n - V}{S_n}\right)},$$

$$\tau_f = \frac{\tau_f^*}{\exp(V_f - V)/2S_f + \exp(V - V_f)/2S_f}$$

and

$$\tau_n = \frac{\tau_n^*}{1 + \exp(V - V_n)/S_n}.$$

The parametric values are: $C_m = 1$, $g_s = 200$, $g_K = 250$, $g_L = 13$, $V_s = 40$, $V_K = -80$, $V_L = -60$, $V_d = -18$, $S_d = 8$, $V_f = -40$, $S_f = -10$, $V_n = -5$, $S_n = 10$, $\tau_f* = 40$, and $\tau_n^* = 0.0115$. The two bifurcation parameters that give rise to the interesting bursting and chaos behaviors are V_f and τ_n^*.

Model D. This model appeared in Chay [1990 b,c]. As in Model C, f depends on time and voltage. However, unlike models A, B, and C, the spike is generated by $[Ca^{2+}]_i$ which is a fast dynamic variable in this model. That is, $[Ca^{2+}]_i$ affects h_∞ (the fast inactivating component of the Ca^{2+} current) and n_∞ (the probability of opening of the

K–Ca channel), and n_∞ together with h_∞ generate a spike. The three simultaneous equations in the model are expressed as follows:

$$-C_m\frac{dV}{dt} = g_{\mathrm{Ca}}d_\infty f h_\infty(V-V_{\mathrm{Ca}}) + g_{\mathrm{K},C}n_\infty(V-V_{\mathrm{K}}) + g_L(V-V_L),$$

$$\frac{df}{dt} = \frac{f_\infty - f}{\tau_f},$$

$$\frac{d[\mathrm{Ca}^{2+}]_{\mathrm{i}}}{dt} = \frac{d_\infty f h_\infty(V_{\mathrm{Ca}}-V) - k_C[\mathrm{Ca}^{2+}]_{\mathrm{i}}}{\tau_C},$$

where

$$d_\infty = \frac{1}{1+\exp\left(\frac{V_d - V}{S_d}\right)}$$

and

$$n_\infty = \frac{1}{1+\exp\left(\frac{V_n - V}{S_n}\right)},$$

$$f_\infty = \frac{1}{1+\exp\left(\frac{V_f - V}{S_f}\right)}$$

and

$$\tau_f = \frac{\tau_f^*}{\exp(V_f - V)/2S_f + \exp(V - V_f)/2S_f},$$

$$h_\infty = \frac{1}{1+C} \quad \text{where} \quad C = \frac{[\mathrm{Ca}^{2+}]_{\mathrm{i}}}{K_h},$$

$$V_n = -35\ln\left(\frac{[\mathrm{Ca}^{2+}]_{\mathrm{i}}}{K_n}\right).$$

The parametric values are: $C_m = 1$, $g_{\mathrm{Ca}} = 400$, $g_{\mathrm{K},C} = 9000$, $g_L = 25$, $V_{\mathrm{Ca}} = 100$, $V_{\mathrm{K}} = -90$, $V_L = -60$, $V_d = -13$, $S_d = 8$, $V_f = -40$, $S_f = -10$, $S_n = 13$, $\tau_f^* = 40$, $\tau_C = 0.06$, $k_C = 2$, $K_h = 1$, and $K_n = 10$. Note here that (unlike Models A and B) V_n is not constant but is a function of $[\mathrm{Ca}^{2+}]_{\mathrm{i}}$. The two bifurcation parameters that give rise to the interesting bursting and chaos behaviors are V_f and τ_C.